

1 **Statistics and Forecasting of Aftershocks during the**
2 **2019 Ridgecrest, California, Earthquake Sequence**

3 **Robert Shcherbakov^{1,2}**

4 ¹Department of Earth Sciences, University of Western Ontario, London, Ontario, *N6A 5B7*, Canada.

5 ²Department of Physics and Astronomy, University of Western Ontario, London, Ontario, *N6A 3K7*,
6 Canada.

7 **Key Points:**

- 8 • Statistical analysis of the 2019 Ridgecrest, California, earthquake sequence is per-
9 formed.
- 10 • The probabilities for the occurrence of the largest expected aftershocks are com-
11 puted using the Bayesian predictive framework.
- 12 • The aftershock forecast is verified retrospectively using several statistical tests.

Abstract

The 2019 Ridgecrest, California, earthquake sequence represents a complex pattern of seismicity that is characterized by the occurrence of a well defined foreshock sequence followed by a mainshock and subsequent aftershocks. In this work, a detailed statistical analysis of the sequence is performed. Particularly, the parametric modelling of the frequency-magnitude statistics and the earthquake occurrence rate is carried out. It is shown that the clustering of earthquakes plays an important role during the evolution of this sequence. In addition, the problem of constraining the magnitude of the largest expected aftershocks to occur during the evolution of the sequence is addressed. In order to do this, two approaches are considered. The first one is based on the extreme value theory, whereas the second one uses the Bayesian predictive framework. The latter approach has allowed to incorporate the complex earthquake clustering through the Epidemic Type Aftershock Sequence (ETAS) process and the uncertainties associated with the model parameters into the computation of the corresponding probabilities. The results indicate that the inclusion of the foreshock sequence into the analysis produces higher probabilities for the occurrence of the largest expected aftershocks after the M7.1 mainshock compared to the approach based on the extreme value distribution combined with the Omori-Utsu formula for the earthquake rate. Several statistical tests are applied to verify the forecast.

Plain Language Summary

Strong earthquakes typically trigger the subsequent sequence of events known as aftershocks. Among those, the largest aftershocks can pose significant hazard and result in additional damage to infrastructure already weakened by the mainshock. Therefore, the estimation of the magnitude of the largest expected aftershock is of critical importance. This problem can be addressed within the statistical modelling of the occurrence of earthquakes. In this work, the 2019 Ridgecrest, California, earthquake sequence is chosen to illustrate and compare several approaches to constrain the magnitudes of the largest expected aftershocks during the evolution of the sequence. The first approach uses the extreme value theory and the modelling of the earthquake rate based on the Omori-Utsu formula. Whereas, the second approach uses a recently formulated method based on the Bayesian predictive analysis and the Epidemic Type Aftershock Sequence (ETAS) model to approximate the earthquake rate. The obtained results indicate that the latter ap-

45 proach produces statistically accurate forecast for the magnitudes of the largest expected
46 earthquakes. This is verified by applying several statistical tests.

47 **1 Introduction**

48 The occurrence of a significant mainshock presents an opportunity to test differ-
49 ent existing or novel statistical approaches to model the evolution of the corresponding
50 sequences of earthquakes that precede and follow the mainshock. Among several statis-
51 tical measures, the computation of the probability to have the magnitude of the largest
52 expected earthquake to be above a certain value during a predefined future time inter-
53 val is of critical importance. In this respect, the 2019 Ridgecrest, California, earthquake
54 sequence represents the latest highly productive and non-standard sequence to be an-
55 alyzed in detail.

56 The problem of constraining the magnitudes of the largest expected aftershocks is
57 important as these aftershocks can inflict further damage to already weakened by a main-
58 shock structures or the evolution of the sequence can trigger even larger subsequent events
59 (Gerstenberger et al., 2005; Shebalin et al., 2011; Omi et al., 2013; Page et al., 2016).
60 The standard approach is to use the past seismicity to compute the probabilities of hav-
61 ing subsequent strong earthquakes during a finite future time interval. The most recog-
62 nized model was formulated by Reasenberg and Jones (1989) for California based on the
63 analysis of the past aftershock sequences. In that model, the probabilities are computed
64 from the extreme value distribution by assuming that the occurrence of earthquakes fol-
65 lows a non-homogeneous Poisson process, the earthquake rate is approximated by the
66 Omori-Utsu formula and the frequency-magnitude statistics is described by the left-truncated
67 exponential distribution. Reasenberg and Jones (1989) estimated the average values of
68 the model parameters to be used in California. However, a recent work by Hardebeck
69 et al. (2019) introduced improvements to the original model by analysing more recent
70 sequences, introducing the ability to control the early incompleteness of aftershock se-
71 quences, and using the Bayesian updating of the model parameters. These developments
72 contributed to the introduction of the operational aftershock forecasting in the U.S. by
73 the U.S. Geological Survey (Michael et al., 2019). A similar approach has been under-
74 taken in Japan to create a real-time system for automatic aftershock forecasting (Omi
75 et al., 2016, 2019). Earthquake forecasting centers also operate in New Zealand (Rhoades

76 et al., 2018) and Italy (Taroni et al., 2018), where the evaluation of earthquake proba-
77 bilities and assessment of earthquake hazard are routinely performed.

78 A critical aspect of any earthquake forecasting methods is their prospective/retrospective
79 testing and validation (Kagan & Jackson, 1995). This is consistently implemented by
80 the Collaboratory for the Study of Earthquake Predictability (CSEP) (Schorlemmer et
81 al., 2007; Zechar et al., 2010; Schorlemmer et al., 2018; Gerstenberger et al., 2020). Within
82 the CSEP framework several statistical methods were developed to test the short/long
83 term earthquake forecasts. Those methods test the consistency of a given forecasting scheme
84 to reproduce the observed number of earthquakes, their spatial and magnitude distri-
85 butions during the forecasting time interval (Zechar et al., 2010). They also incorporate
86 likelihood based approaches to compare various forecasting schemes. For example, this
87 framework was used to test the performance of aftershock forecasts during the 2011 To-
88 hoku, Japan, earthquake (Nanjo et al., 2012), the 2010 Canterbury, New Zealand, earth-
89 quake sequence (Rhoades et al., 2016; Cattania et al., 2018), and the 2016 Kaikoura, New
90 Zealand, earthquake sequence (Rhoades et al., 2018).

91 An early systematic empirical study of aftershocks concluded that the largest oc-
92 curred aftershock on average was approximately 1.2 magnitude less than the magnitude
93 of a mainshock (Båth, 1965). This is referred to as Båth's law. Subsequently, it was pro-
94 posed that the difference was independent of the number of events and its mean value
95 was proportional to the inverse of the b -value (Vere-Jones, 1969, 1975). More recent stud-
96 ies have provided further details on this difference (Console et al., 2003; Shcherbakov &
97 Turcotte, 2004; Tahir et al., 2012; Shearer, 2012; Shcherbakov et al., 2013). The after-
98 shock sequences also exhibit scaling with respect to the lower magnitude cutoff (Shcherbakov
99 et al., 2004; Shcherbakov, Turcotte, & Rundle, 2005; Shcherbakov et al., 2006, 2015).

100 An important limitation of all earthquake catalogs is the early aftershock incom-
101 pleteness (Kagan, 2004; Peng et al., 2006; Hainzl, 2016b, 2016a). This incompleteness
102 can affect the estimation of the model parameters if the magnitude of completeness is
103 underestimated. As a result, this can significantly influence the calculation of the prob-
104 abilities for the occurrence of extreme earthquakes. To recover partially the true rate a
105 variable magnitude of completeness can be considered (Helmstetter et al., 2006; Omi et
106 al., 2014; Page et al., 2016). Several approaches were suggested to recover the aftershock
107 rate by using the information of early aftershocks in order to estimate the probability

108 of larger subsequent events during future evolution of the sequences (Omi et al., 2013;
109 Ebrahimian et al., 2014; Omi et al., 2016).

110 The occurrence of strong earthquakes typically produces spatial and temporal clus-
111 ters. This clustering is a result of triggering by preceding earthquakes that can lead to
112 a cascade of events with a complicated branching structure (Felzer et al., 2004). To de-
113 scribe such a clustering, the ETAS model was introduced that offers a realistic and quan-
114 tifiable approximation to the earthquake occurrence rate (Ogata, 1988, 1999, 2017). Par-
115 ticularly, it can model the rate of earthquakes punctuated by the occurrence of strong
116 earthquakes. This also allows to quantify the increased earthquake hazard after a main-
117 shock by incorporating the triggering ability of foreshocks, a mainshock, and subsequent
118 aftershocks. It also can be used for short-term forecasting of large earthquakes by study-
119 ing past seismicity (Helmstetter et al., 2006; Werner et al., 2011; Ogata, 2017; Ebrahimian
120 & Jalayer, 2017; Harte, 2017; Omi et al., 2019).

121 After the occurrence of the 2019 Ridgecrest earthquakes, several approaches have
122 been used to study the statistical and triggering aspects of this sequence. The operational
123 earthquake forecasting was documented based on the UCERF3-ETAS model (Milner et
124 al., 2020; Savran et al., 2020). Retrospective analysis of the historic seismicity in Cal-
125 ifornia and its relation to the initiation of the 2019 Ridgecrest sequence was performed
126 (Ogata & Omi, 2020). Predictive skills of the models based on the Coulomb stress trans-
127 fer were analyzed (Mancini et al., 2020; Toda & Stein, 2020). The triggering of aftershocks
128 during the evolution of the sequence was studied using the stress-similarity model (Hardebeck,
129 2020). The question of changes in the stress field inferred from past seismicity and its
130 relation to the initiation of the Ridgecrest sequence and subsequent relaxation was ad-
131 dressed in Nanjo (2020).

132 In this paper, a detailed statistical analysis of the 2019 Ridgecrest earthquake se-
133 quence was performed to study its temporal evolution and frequency-magnitude statis-
134 tics. In addition, several methods were considered to estimate the probabilities to have
135 the largest expected aftershock to be above a certain magnitude during several stages
136 of the evolution of the sequence. The computation of probabilities was performed using
137 two approaches, i.e., the one based on the extreme value theory and the second one us-
138 ing the Bayesian predictive distribution. These approaches assume parametric models
139 for the earthquake occurrence rate and the frequency-magnitude statistics. Specifically,

140 the Omori-Utsu (OU) law (Omori, 1894; Utsu, 1961; Utsu et al., 1995), the compound
141 Omori-Utsu law (Ogata, 1983), and the Epidemic Type Aftershock Sequence (ETAS)
142 process (Ogata, 1988, 1999, 2017) were used to approximate the earthquake rate. The
143 frequency-magnitude statistics of earthquakes was modelled by the left-truncated expo-
144 nential distribution (Vere-Jones, 2010). The obtained results, which are reported below,
145 suggest that the clustering of earthquakes plays an important role in approximating the
146 earthquake rate and as a consequence can significantly affect the computation of the prob-
147 abilities for the occurrence of the largest expected aftershocks.

148 The paper is organized as follows. In Section 2, the statistical methods used in the
149 study are summarized and explained. In Section 3, a detailed analysis of the sequence
150 is presented. The retrospective validation of the forecasting results is given in Section
151 4. In Section 5, the obtained results are summarized and evaluated. The last section presents
152 concluding remarks.

153 **2 Data and Methods**

154 **2.1 The 2019 Ridgecrest earthquake sequence**

155 The 2019 Ridgecrest earthquake sequence started on July 4th when several small
156 events of low magnitude occurred not far away from the town of Ridgecrest in Califor-
157 nia. Then, two strong foreshocks of magnitudes M3.98 and M6.4 struck on 2019/07/04
158 at 17:02:55 UTC and 17:33:49 UTC, respectively (Figure 1). These events were followed
159 by a well-developed aftershock sequence that culminated in the occurrence of M7.1 main-
160 shock on 2019/07/06 (03:19:53 UTC), which in turn generated a more prolific aftershock
161 sequence. The M6.4 foreshock ruptured several predominantly strike-slip, left-lateral fault
162 segments, whereas the M7.1 mainshock occurred on a system of several right-lateral fault
163 segments conjugate to the rupture of the M6.4 foreshock (Ross et al., 2019; Barnhart et
164 al., 2019). Many of the foreshocks and subsequent aftershocks of the M7.1 mainshock
165 occurred on numerous secondary faults adjacent to the main rupture faults. It was sug-
166 gested that this earthquake sequence occurred in an immature fault zone with a com-
167 plex fault structure (Ross et al., 2019; Liu et al., 2019).

168 To analyze the 2019 Ridgecrest earthquake sequence, the earthquake catalog pro-
169 vided by the Southern California Seismic Network (SCSN, 2020) was used. The spatial
170 distribution of seismicity during 14 days starting from 2019/07/04 (17:02:55 UTC) is shown

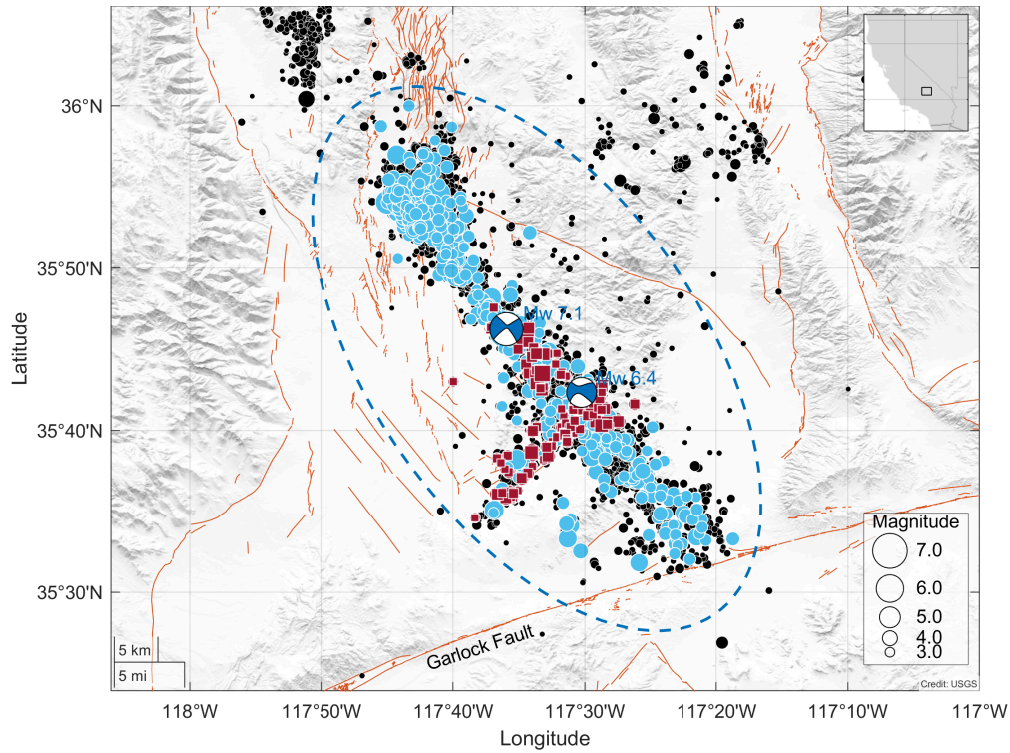


Figure 1. The distribution of earthquake epicenters of the 2019 Ridgecrest, California, sequence during 14 days starting from 2019/07/04 (17:02:55 UTC). Dark red solid squares within an elliptical zone indicate foreshocks above magnitude $m \geq 3.2$ during 1.428 days before the occurrence of the M7.1 mainshock on 2019/07/06 (03:19:53 UTC). Similarly, blue solid circles indicate aftershocks of the M7.1 mainshock. The focal mechanisms of the M7.1 mainshock and M6.4 foreshock are plotted as beach balls. All other earthquakes above magnitude $m \geq 2.0$ are shown as black solid circles. The quaternary faults are plotted as light brown line segments.

171 in Figure 1. This includes the occurrence of the M6.4 foreshock on 2019/07/04 (17:33:49
 172 UTC) and the occurrence of the M7.1 mainshock on 2019/07/06 (03:19:53 UTC). Their
 173 focal mechanisms are also shown and were obtained from the SCSN Moment Tensor cat-
 174 alog (SCSN, 2020). The foreshock-aftershock zone for the sequence is defined as an el-
 175 liptical region outlining the majority of earthquakes that occurred near the ruptures of
 176 both the M6.4 foreshock and M7.1 mainshock. Figure 1 also shows the quaternary faults
 177 for this region extracted from the U.S.G.S. Quaternary fault and fold database (USGS,
 178 2006).

179 When analyzing seismicity, several time intervals, during which the parameters of
 180 statistical models can be estimated or future evolution of the seismicity can be quanti-
 181 fied, are defined. Specifically, the past seismicity is extracted during the *training time*
 182 *interval* $[T_0, T_e]$. To minimize the effect of earlier earthquakes in the sequence, the train-
 183 ing time interval is typically subdivided into a preparatory time interval $[T_0, T_s]$ and a
 184 *target time interval* $[T_s, T_e]$ during which the parameters of the earthquake models are
 185 estimated. One also considers a *forecasting time interval* $[T_e, T_e + \Delta T]$ during which
 186 specific measures of seismicity can be computed or evolution of seismicity can be fore-
 187 casted. For properly estimating the parameters of earthquake models, it is also impor-
 188 tant to consider the seismicity above the magnitude of completeness m_c as typical earth-
 189 quake catalogs have missing events below this magnitude.

190 For the statistical modeling of seismicity, the occurrence of earthquakes can be con-
 191 sidered as a realization of a stochastic marked point process in time (Daley & Vere-Jones,
 192 2003; Vere-Jones, 2010). In this representation, the earthquakes are characterized by their
 193 occurrence times t_i and magnitudes m_i represent corresponding marks. The occurrence
 194 of earthquakes during a specified time interval can be arranged in an ordered set $\mathbf{S} =$
 195 $\{(t_i, m_i)\} : i = 1, \dots, n$. In one simplified assumption, the occurrence of earthquakes
 196 in the sequence can be described by a non-homogeneous Poisson marked point process
 197 (Utsu et al., 1995; Shcherbakov, Yakovlev, et al., 2005), where magnitudes and the time
 198 intervals between successive events are not correlated.

2.2 Exponential Distribution and the Gutenberg-Richter Scaling Relation

The frequency-magnitude statistics of earthquake magnitudes is typically modelled by the left-truncated exponential distribution (Vere-Jones, 2010):

$$f_{\theta}(m) = \beta \exp[-\beta(m - m_0)], \quad (1)$$

$$F_{\theta}(m) = 1 - \exp[-\beta(m - m_0)], \quad \text{for } m \geq m_0, \quad (2)$$

where $f_{\theta}(m)$ is the probability density, $F_{\theta}(m)$ is the cumulative distribution function, and $\theta = \{\beta\}$ is the model parameter. m_0 is a given lower magnitude cutoff set above the catalog completeness level $m_0 \geq m_c$. All earthquakes above m_0 during the target time interval $[T_s, T_e]$ are used to estimate the model parameter β .

The parameter β is related to the b -value of the Gutenberg-Richter (GR) scaling relation, $\beta = \ln(10)b$ (Gutenberg & Richter, 1944):

$$\log_{10} N(\geq m) = a - b m, \quad (3)$$

where $N(\geq m)$ is the cumulative number of earthquakes above magnitude m . The GR relation combines two aspects of the occurrence of earthquakes, i.e. the frequency-magnitude statistics of earthquake magnitudes and the average rate of the occurrence of earthquakes, which is quantified through the parameter a . $N(\geq 0) = 10^a$ gives the total number of earthquakes above magnitude zero that occurred during the corresponding time interval.

The standard method to estimate the parameter β (or b -value) is to use the maximum likelihood approach, which has an analytic solution for the point estimator of the parameter of the exponential distribution. However, in typical earthquake catalogs the magnitudes are binned and not continuous variables. Therefore, one needs to apply a corrected estimator, which explicitly assumes the binning of the magnitudes (Bender, 1983). For the estimation of the parameter uncertainties at a given confidence level in case of binned magnitudes one can use the method suggested in Tinti and Mulargia (1987).

2.3 Omori-Utsu Law

The occurrence of moderate to large earthquakes, in most cases, triggers subsequent aftershock sequences and results in the rise of seismic activity. The most accepted model

225 that reproduces the rate of the occurrence of aftershocks is known as the Omori-Utsu (OU)
 226 law (Omori, 1894; Utsu, 1961; Utsu et al., 1995):

$$\lambda_{\omega}(t) = \frac{K_o}{(t + c_o)^{p_o}}, \quad (4)$$

227 where λ_{ω} is the rate of aftershocks per unit time for events above a certain magnitude
 228 m_0 . $\omega = \{K_o, c_o, p_o\}$ are the OU model parameters. The time t is elapsed since $T_0 =$
 229 0, which corresponds to the time of the occurrence of the mainshock. The parameter K_o
 230 describes the productivity of the sequence, c_o is a characteristic time, and p_o specifies
 231 how fast or slow the sequence decays in time. The parameters can be estimated using
 232 the maximum likelihood method and parameter uncertainties are computed using the
 233 inverse of the Fisher information matrix, which is derived from the likelihood function
 234 (Ogata, 1983, 1999). In this model, it is assumed that the occurrence of earthquakes can
 235 be approximated by a non-homogeneous Poisson process, where earthquake magnitudes
 236 are independent and identically distributed (i.i.d.) random numbers and do not influ-
 237 ence the future earthquake rate. The Bayesian approach to estimate the parameters and
 238 their uncertainties of the OU law was also implemented (Holschneider et al., 2012).

239 The Omori-Utsu law is applicable to "standard" aftershock sequences with a sin-
 240 gle mainshock and a consistently decaying rate. However, in some cases the earthquake
 241 sequence can be punctuated by several strong shocks each one of them producing their
 242 own aftershocks. In that case, a compound Omori-Utsu model can be considered (Ogata,
 243 1983; Shcherbakov et al., 2012). In a case of two strong earthquakes, it is written as:

$$\lambda_{\omega}(t) = \frac{K_1}{(t + c_1)^{p_1}} + H(t - \tau_m) \frac{K_2}{(t - \tau_m + c_2)^{p_2}}, \quad (5)$$

244 where $\omega = \{K_1, c_1, p_1, K_2, c_2, p_2\}$, time t is elapsed since the occurrence of the first
 245 event at $T_0 = 0$ and τ_m is the time of the occurrence of the second strong event. $H(x)$
 246 is a Heaviside step function and is equal to one for positive $x \geq 0$ and is zero otherwise.
 247 For the times past the occurrence of the second strong earthquake ($t \geq \tau_m$), Eq. (5)
 248 defines the earthquake rate as a superposition of two aftershock sequences triggered by
 249 the both strong earthquakes.

250 2.4 Epidemic Type Aftershock Sequence (ETAS) Model

251 The occurrence of earthquakes is characterized by the clustering of seismicity. This
 252 clustering is a direct manifestation of the ability of earthquakes to trigger subsequent

253 events. The ETAS model was introduced to reflect this essential aspect of the occurrence
 254 of earthquakes (Ogata, 1988, 1999, 2017). In the temporal version of the model, the con-
 255 ditional earthquake rate $\lambda_\omega(t|\mathcal{H}_t)$ at a given time t is given as (Ogata, 1988; Harte, 2010):

$$\lambda_\omega(t|\mathcal{H}_t) = \mu + K \sum_{i:t_i < t}^{N_t} \frac{e^{\alpha(m_i - m_0)}}{\left(\frac{t-t_i}{c} + 1\right)^p}, \quad (6)$$

256 where $\omega = \{\mu, K, c, p, \alpha\}$ is a set of parameters and m_0 is a reference magnitude. The
 257 summation is performed over the history, \mathcal{H}_t , of past events up to time t during the time
 258 interval $[T_0, t]$. N_t is the number of earthquakes in the interval $[T_0, t]$ above the lower
 259 magnitude cutoff m_0 . In the ETAS process, a certain fraction of earthquakes occurs ran-
 260 domly with a constant rate μ . These earthquakes are associated with background seis-
 261 micity driven by tectonic loading and can be modelled as a homogeneous Poisson pro-
 262 cess. It is also postulated that each earthquake is capable of triggering its own offsprings.
 263 As a result, the total earthquake rate at a given time, is a superposition of the background
 264 rate given by μ and the contribution from each already occurred earthquake.

265 As the ETAS rate, Eq. (6), is conditioned on past seismicity \mathcal{H} , one has to min-
 266 imize the effect of lack of earthquakes at the start of the sequence when estimating the
 267 ETAS parameters. For this, one can consider a short time interval $[T_0, T_s]$ before the tar-
 268 get time interval $[T_s, T_e]$. The earthquakes in the interval $[T_0, T_s]$ can be used to prop-
 269 erly estimate the conditional earthquake rate during the target time interval $[T_s, T_e]$. The
 270 explicit forms of the log-likelihood function and the productivity of the ETAS model were
 271 given in Shcherbakov et al. (2019). The ETAS parameters $\omega = \{\mu, K, c, p, \alpha\}$ are es-
 272 timated in the target time interval $[T_s, T_e]$ by maximizing the likelihood function and
 273 the uncertainties are computed using the inverse of the Fisher information matrix.

274 2.5 Extreme Value Distribution

275 For the sequence of earthquake that can be described as a non-homogeneous Pois-
 276 son process, the probability that the magnitude of the largest expected event will exceed
 277 m for all possible number of events during a future time interval $[T_e, T_e + \Delta T]$ can be
 278 computed from the extreme value distribution (EVD) (Campbell, 1982; Coles, 2001; Da-
 279 ley & Vere-Jones, 2003):

$$P_{\text{EV}}(m_{\text{ex}} > m|\theta, \omega, \Delta T) = 1 - \exp\{-\Lambda_\omega(\Delta T) [1 - F_\theta(m)]\}, \quad (7)$$

280 where the productivity is $\Lambda_\omega(\Delta T) = \int_{T_e}^{T_e + \Delta T} \lambda_\omega(t) dt$. Using the exponential model for
 281 the magnitude distribution, Eq. (2), this results in the Gumbel distribution for the mag-

282 nitudes of extreme earthquakes:

$$P_{\text{EV}}(m_{\text{ex}} > m|\theta, \omega, \Delta T) = 1 - \exp\{-\Lambda_{\omega}(\Delta T) \exp[-\beta(m - m_0)]\}. \quad (8)$$

283 Assuming that the earthquake rate is described by the OU law (4), the productiv-
284 ity $\Lambda_{\omega}(\Delta T)$ can be computed explicitly and takes the following form for $p_o \neq 1$:

$$\Lambda_{\omega}(\Delta T) = K_o \frac{(T_e + c_o)^{1-p_o} - (T_e + \Delta T + c_o)^{1-p_o}}{p_o - 1}. \quad (9)$$

285 Given a set of parameters $\{\theta, \omega\}$, which can be estimated from past seismicity during
286 the training time interval $[T_s, T_e]$, Eqs. (8) and (9) allow to compute the probability to
287 have the extreme earthquake above magnitude m during a future time interval ΔT . It
288 is equivalent to the computation of the probabilities given in Reasenberg and Jones (1989).

289 For the compound OU model (5) the productivity $\Lambda_{\omega}(\Delta T)$ can be expressed as fol-
290 lows for $p_1 \neq 1$ and $p_2 \neq 1$:

$$\Lambda_{\omega}(\Delta T) = K_1 \frac{(T_e + c_1)^{1-p_1} - (T_e + \Delta T + c_1)^{1-p_1}}{p_1 - 1} + K_2 \frac{(T_e - \tau_m + c_2)^{1-p_2} - (T_e + \Delta T - \tau_m + c_2)^{1-p_2}}{p_2 - 1}, \quad (10)$$

291 where τ_m is the time of the occurrence of the second strong earthquake during the train-
292 ing time interval $[T_s, T_e]$.

293 2.6 Bayesian Predictive Distribution

294 The computation of the EVD (7) using specific parametric models for the earth-
295 quake rate and frequency-magnitude statistics, requires the knowledge of the model pa-
296 rameters. However, the true values of the model parameters are not known for specific
297 earthquake sequences. As a result, the parameter estimates are used, which are computed
298 with a given range of uncertainties. Those uncertainties can significantly affect the com-
299 putation of the corresponding probabilities. The incorporation of the model uncertain-
300 ties into the computation of probabilities can be achieved through the Bayesian predic-
301 tive distribution (BPD) (Zöller et al., 2013; Shcherbakov et al., 2018, 2019). The BPD
302 for the largest expected event m_{ex} to be greater than a certain value m and during the
303 forecasting time interval ΔT is:

$$P_{\text{B}}(m_{\text{ex}} > m|\mathbf{S}, \Delta T) = \int_{\Omega} \int_{\Theta} P_{\text{EV}}(m_{\text{ex}} > m|\theta, \omega, \Delta T) p(\theta, \omega|\mathbf{S}) d\theta d\omega, \quad (11)$$

304 where Θ and Ω define the multidimensional domains of the frequency-magnitude distri-
 305 bution and earthquake rate parameters, respectively. When computing the predictive
 306 distribution, Eq. (11), the model parameter uncertainties are fully integrated into the
 307 BPD (Renard et al., 2013; Shcherbakov et al., 2019). This is done through the use of the
 308 posterior distribution function $p(\theta, \omega | \mathbf{S})$, which characterizes the distribution of the model
 309 parameter uncertainties.

310 For the ETAS model, the extreme value distribution for the extreme events does
 311 not follow Eq. (7), due to stochastic nature of the process, which deviates from a non-
 312 homogeneous Poisson process. In this case, one can compute the extreme value distri-
 313 bution by stochastic simulation of the ETAS model and extracting the maximum mag-
 314 nitude from each simulated sequence (Shcherbakov et al., 2019).

315 To compute the BPD (11) for a given training time interval, first, the Markov Chain
 316 Monte Carlo (MCMC) sampling of the posterior distribution is performed to generate
 317 a chain of the ETAS parameters using the Metropolis-within-Gibbs algorithm. The gen-
 318 erated chains of length N_{sim} are used to simulate the ensemble of the ETAS processes
 319 forward in time during the forecasting time interval ΔT . From each simulated sequence
 320 the maximum event is extracted and the distribution of these maxima approximates the
 321 BPD (Shcherbakov et al., 2019).

322 **3 Results**

323 **3.1 Frequency-Magnitude Statistics**

324 The earthquakes within an elliptical region, given in Figure 1, were extracted dur-
 325 ing predefined target time intervals. The frequency-magnitude statistics of earthquake
 326 magnitudes were computed for the foreshock sequence starting from 2019/07/04 (17:02:55
 327 UTC) which corresponds to $T_0 = 0$ and during the target time interval $[T_s, T_e] = [10^{-4}, 1.428]$
 328 days. It was also computed for the aftershocks of the M7.1 mainshock starting from 2019/07/06
 329 (03:19:53 UTC) during 7 days after the mainshock. The frequency-magnitude statistics
 330 was also computed for the whole sequence including both foreshocks and aftershocks dur-
 331 ing 31 days. The results are given in Figure 2 as open symbols for events larger than $m \geq$
 332 2.0. The maximum likelihood fits of the exponential distribution, Eq. (2), to the frequency-
 333 magnitude data above $m \geq 3.2$ are shown as GR plots with estimated b -values using

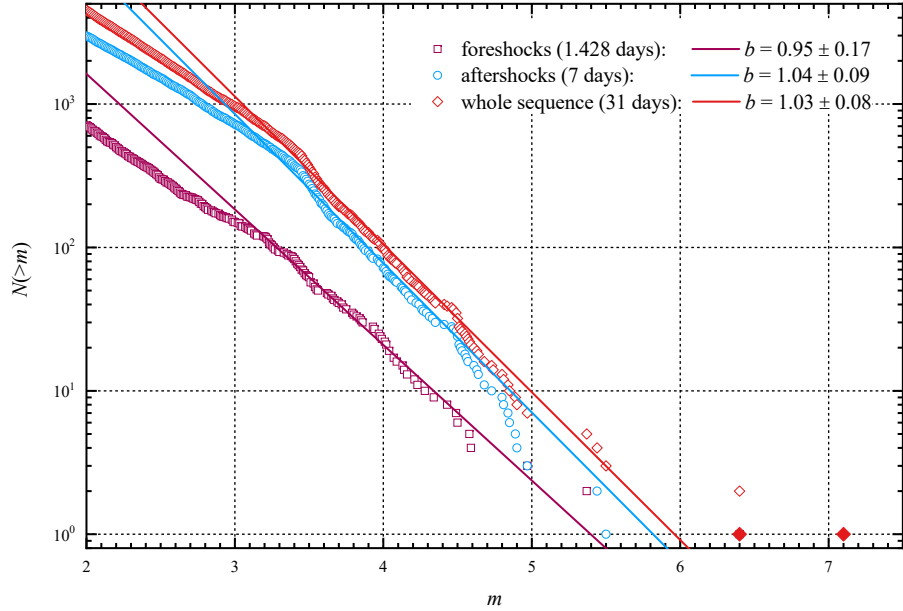


Figure 2. The frequency-magnitude statistics of earthquakes in the sequence and the modelling by the Gutenberg-Richter relation, Eq. (3). The symbols (representing the cumulative numbers) correspond to the foreshocks of the M7.1 mainshock (open squares), the aftershocks of the mainshock (open circles), and for the whole sequence (open diamonds). The fits of the GR relation are plotted as straight lines. The estimated b -values are given in the legend for all earthquakes above $m \geq 3.2$. The uncertainties are given as 95% confidence intervals.

334 the method of Bender (1983) and their 95% confidence intervals according to Tinti and
 335 Mulargia (1987).

336 The sequence exhibited a change in the slope of the frequency-magnitude statis-
 337 tics around a magnitude 3.2. This was the reason to use only the events above this value
 338 in the analysis. This change in the behavior can be the result of the early aftershock in-
 339 completeness observed right after the M6.4 foreshock and the M7.1 mainshock or it can
 340 be related to the fact that the aftershocks occurred on a distributed fault network and
 341 the geometrical distribution of fault sizes affected the statistics of earthquake magnitudes.
 342 The fit of the exponential distribution, Eq. (2), (or the corresponding Gutenberg-Richter
 343 relation) to the frequency-magnitude statistics of the foreshock and aftershock sequences
 344 produced the b -values which were typical for tectonic earthquakes as illustrated in Fig-
 345 ure 2. The largest aftershock of the M7.1 mainshock had a magnitude 5.5 and occurred
 346 less than half an hour after the mainshock. Two more strong aftershocks of magnitude

347 4.7 and 5.0 occurred later in the sequence on 20th and 48th days after the mainshock.
 348 The value of the largest occurred aftershock is lower than what would be expected from
 349 Båth's law (Båth, 1965). It is possible that the M6.4 foreshock partially released the ac-
 350 cumulated strain energy in the region and this resulted in a lower magnitude of the largest
 351 occurred aftershock.

352 **3.2 Earthquake Rate Evolution and Modelling**

353 First, the earthquake rate was modelled separately for the foreshock and aftershock
 354 sequences using the OU law (4). The results are given in Figure 3 for all earthquakes above
 355 magnitude $m \geq 3.2$. For the foreshock sequence, the following target time interval was
 356 used $[T_s, T_e] = [10^{-3}, 1.407]$ days with $T_0 = 0$ corresponding to 2019/07/04 (17:33:49
 357 UTC). For the aftershock sequence, $T_0 = 0$ was set to the occurrence of the M7.1 main-
 358 shock on 2019/07/06 (03:19:53 UTC) with the target time interval $[T_s, T_e] = [10^{-3}, 30]$
 359 days. The OU law parameters for the foreshock and aftershock sequences are given in
 360 the legend with the corresponding 95% confidence intervals. The earthquake decay rates
 361 after the M6.4 foreshock and M7.1 mainshock exhibited a consistent pattern observed
 362 in other prominent aftershock sequences. The fit of the OU law (4) produced $p = 0.99 \pm$
 363 0.18 for the foreshock sequence and $p = 1.28 \pm 0.07$ for the aftershock sequence (Fig-
 364 ure 3). The smaller p -value for the foreshock sequence can be the result of a strong M5.36
 365 foreshock that occurred 16.2 hours before the M7.1 mainshock and triggered its own se-
 366 quence of events.

367 Next, the compound OU model (5) was used to fit the sequence starting from the
 368 occurrence of the M6.4 foreshock on 2019/07/04 (17:33:49 UTC) corresponding to $T_0 =$
 369 0 and during the following target time interval $[T_s, T_e] = [10^{-3}, 8.407]$ days. This is
 370 illustrated in Figure 4 and Figure S1. The maximum likelihood fitting of the compound
 371 OU model yielded the following parameters $\{K_1, c_1, p_1, K_2, c_2, p_2\} = \{23.22, 0.0026, 0.93, 40.3, 0.034, 1.59\}$.

372 The ETAS model (6) was fitted to the 2019 Ridgecrest sequence using a number
 373 of target time intervals. In one particular example, the training time interval $[T_s, T_e] =$
 374 $[0.03, 8.428]$ days was used with $T_0 = 0$ corresponding to the start date 2019/07/04 (17:02:55
 375 UTC). The estimated conditional rate, Eq. (6), and the corresponding earthquake mag-
 376 nitudes above $m \geq 3.2$ are plotted in Figure 5 and Figure S2. For comparison, the sep-

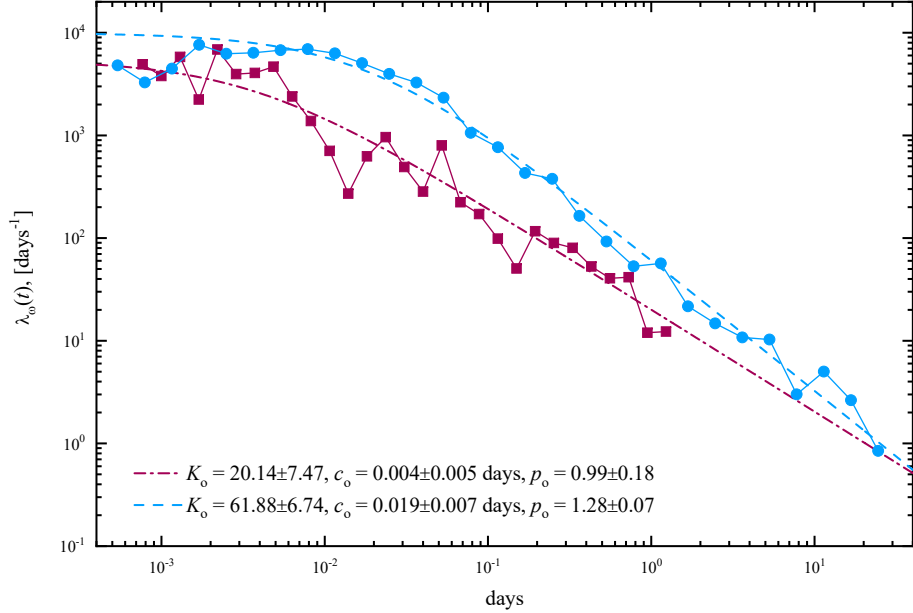


Figure 3. The earthquake decay rates for the foreshock sequence (solid squares) and for the aftershock sequence (solid circles). The corresponding fits of the Omori-Utsu law, Eq. (4), to the foreshock (dash-dotted line) and aftershock (dashed line) sequences. The estimated parameters with the corresponding 95% confidence intervals are given in the legend.

377 arate fits of the Omori-Utsu law to the foreshocks and aftershocks of the M7.1 mainshock
 378 are also plotted with the parameters given in Figure 3.

379 Finally, the point estimates of the model parameters and their 95% confidence in-
 380 tervals were computed at predefined times during the evolution of the sequence (Figure 6).
 381 The reported b -value at time 1.428 days corresponds to the foreshock sequence starting
 382 from the occurrence of the M3.98 event on 2019/07/04 (17:02:55 UTC). The frequency-
 383 magnitude statistics and the fitting of the GR relation to the foreshock sequence is also
 384 illustrated in Figure 2. The subsequent estimates of b -values at days 1d, 2d, etc., cor-
 385 respond to the time duration of the aftershock sequence since the M7.1 mainshock (Fig-
 386 ure 6a). Similarly, the parameters of the OU law (4) were estimated during the same time
 387 intervals (Figure 6b). In addition, the point estimates of the ETAS model parameters
 388 were also computed (Figure 6c). The parameter μ was held constant at $\mu = 0.05$ to im-
 389 prove the stability of the parameter estimation. It was assumed that the background seis-
 390 micity rate for earthquakes above magnitude $m \geq 3.2$ was relatively low in this region
 391 prior to the start of the sequence.

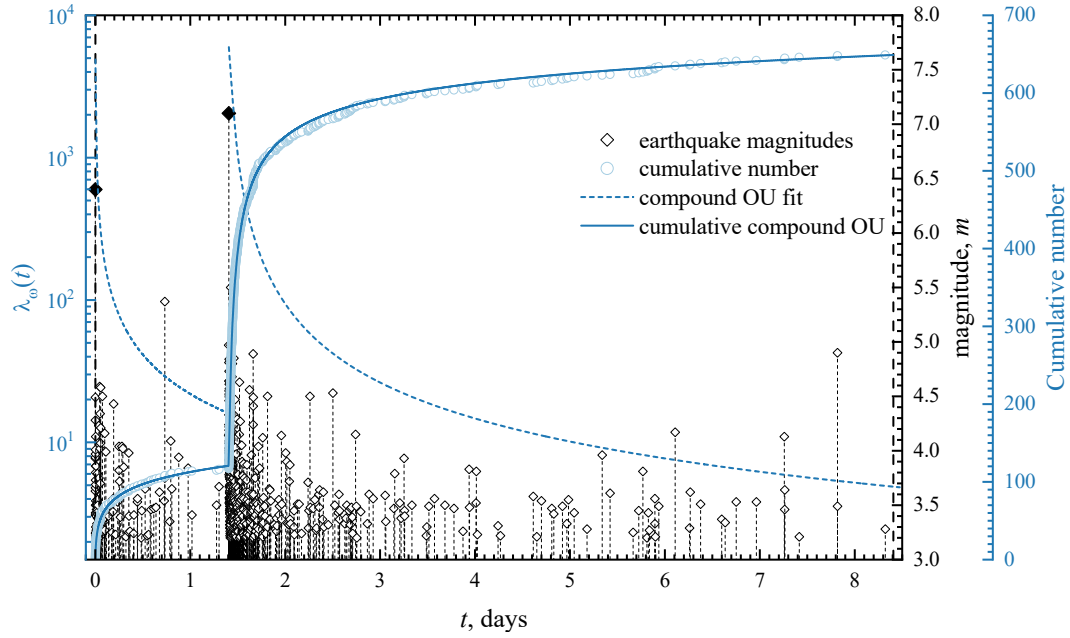


Figure 4. The occurrence of earthquakes during the evolution of the 2019 Ridgecrest sequence and the fitting of the compound Omori-Utsu law, Eq. (5). $T_0 = 0$ corresponds to the occurrence of M6.4 foreshock on 2019/07/04 (17:33:49 UTC). The earthquake magnitudes are plotted as open diamond symbols. The cumulative number of earthquakes is plotted as open circles. The dashed curve corresponds to the fit of the compound Omori-Utsu law, Eq. (5). The corresponding fit of the cumulative numbers is given as a solid curve.

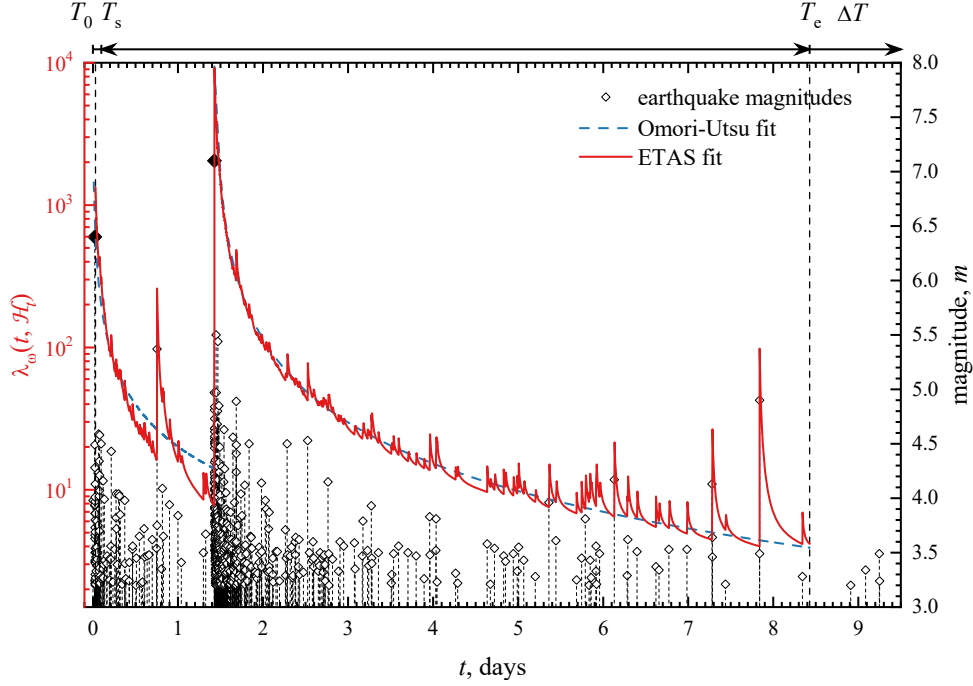


Figure 5. The occurrence of earthquakes during the evolution of the 2019 Ridgecrest sequence and the fitting of the ETAS model, Eq. (6). The start of the sequence $T_0 = 0$ corresponds to the time of the occurrence of the M3.98 foreshock on 2019/07/04 (17:02:55 UTC). The ETAS model is fitted to the sequence during the target time interval $[T_s, T_e] = [0.03, 8.428]$ days. The estimated conditional earthquake rate (solid curve) is plotted using the following ETAS parameters: $\mu = 0.05$, $K = 2.64$, $c = 0.015$, $p = 1.41$, and $\alpha = 2.10$. For comparison, the Omori-Utsu law fit, Eq. (4), is plotted as a short-dashed curve.

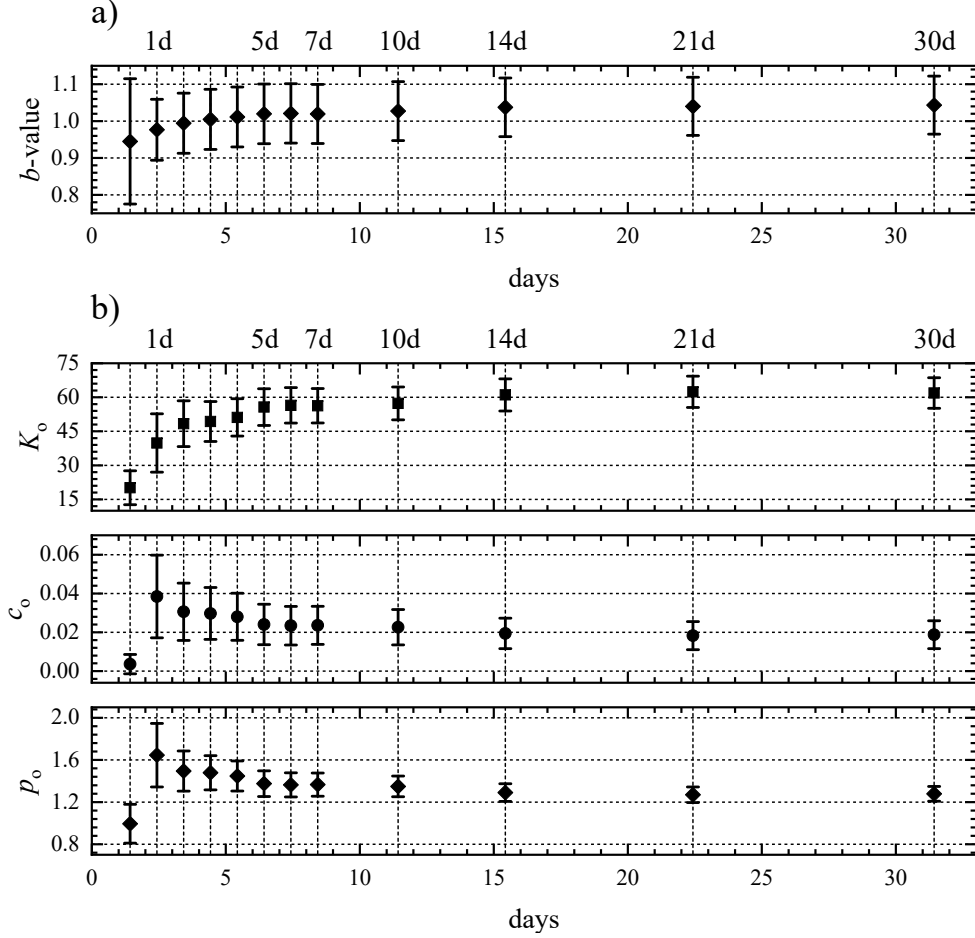


Figure 6. Point estimates of the model parameters during the evolution of the 2019 Ridgecrest sequence. The start of the sequence $T_0 = 0$ corresponds to the time of the occurrence of the M3.98 foreshock on 2019/07/04 (17:02:55 UTC). All the events above magnitude $m \geq 3.2$ were used to compute the parameters using the maximum likelihood method. The point estimates of a) the b -value; b) the Omori-Utsu parameters, Eq. (4), and c) the ETAS parameters, Eq. (6), are plotted. The 95% confidence intervals are also given. The vertical dashed lines correspond to the times in days since the occurrence of the M7.1 mainshock.

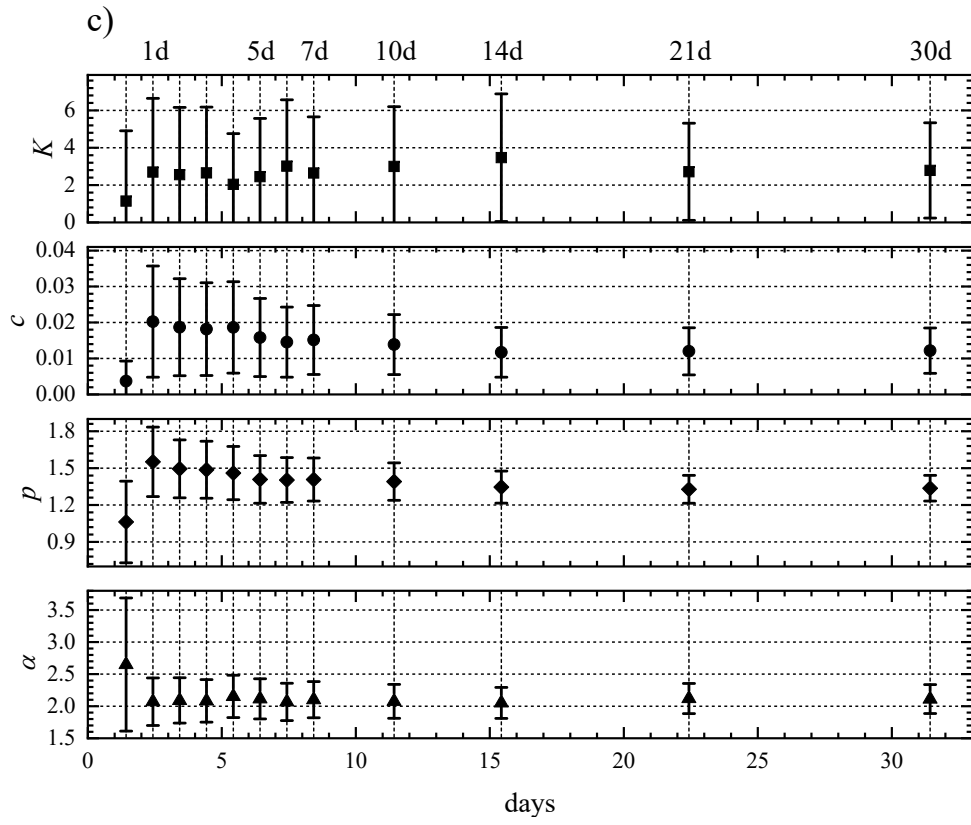


Figure 6. Continued.

3.3 Forecasting the Magnitude of the Largest Expected Earthquake

The EVD (7) and the BPD (11) were used to compute retrospectively the probabilities of having the largest expected earthquakes to occur during predefined times of the evolution of the 2019 Ridgecrest earthquake sequence. This was done both before and after the occurrence of the M7.1 mainshock using the OU (4), compound OU (5), or ETAS (6), parametric models for the earthquake rate and the exponential distribution, Eq. (2), for the distribution of earthquake magnitudes. When computing the probabilities for the aftershock sequence generated by the M7.1 mainshock two cases were analyzed. In the first consideration, only the aftershocks were used. However, when using the ETAS model and the compound OU model the foreshock sequence was also incorporated into the analysis.

First, the only aftershocks of the M7.1 mainshock were used to compute the probabilities of having the strongest aftershocks above a specified magnitude during a future time interval of $\Delta T = 7$ days. The occurrence of the M7.1 mainshock on 2019/07/06 (03:19:53 UTC) corresponded to $T_0 = 0$ with the target time interval $[T_s, T_e] = [10^{-4}, 1]$ days. One particular example is given in Figure 7, where the EVD (8) was computed after 1 day and plotted as a short dashed violet curve. The following model parameter estimates were used: $\{\beta, K_o, c_o, p_o\} = \{2.28, 39.85, 0.038, 1.65\}$. The corresponding probabilities to have strong aftershocks above $m_{\text{ex}} \geq 5.0, 6.1, 7.1$ are also given.

Next, the BPD (11) was computed using the aftershocks of the M7.1 mainshock during different training time intervals to forecast the magnitudes of the largest expected earthquakes to occur during the evolution of the sequence. The OU law (4) was used to approximate the earthquake rate. The exponential distribution, Eq. (2), was used to model the frequency-magnitude statistics. The forecasting time interval was fixed at $\Delta T = 7$ days. The computed BPD to estimate probabilities for the largest expected aftershocks above magnitude $m \geq 3.2$ during one day after the mainshock is plotted in Figure 7 as a dash-dotted cyan curve. This was done by employing the MCMC sampling of the posterior distribution and the Gamma distribution for the priors of the model parameters (Shcherbakov et al., 2019). The total number of 200,000 MCMC sampling steps were performed for each model. The first 100,000 steps were discarded as "burn in" and the remaining $N_{\text{sim}} = 100,000$ sampling steps were used for the synthetic model simulations or analysis. For the OU model, this is given in Figure S3. The distribution of

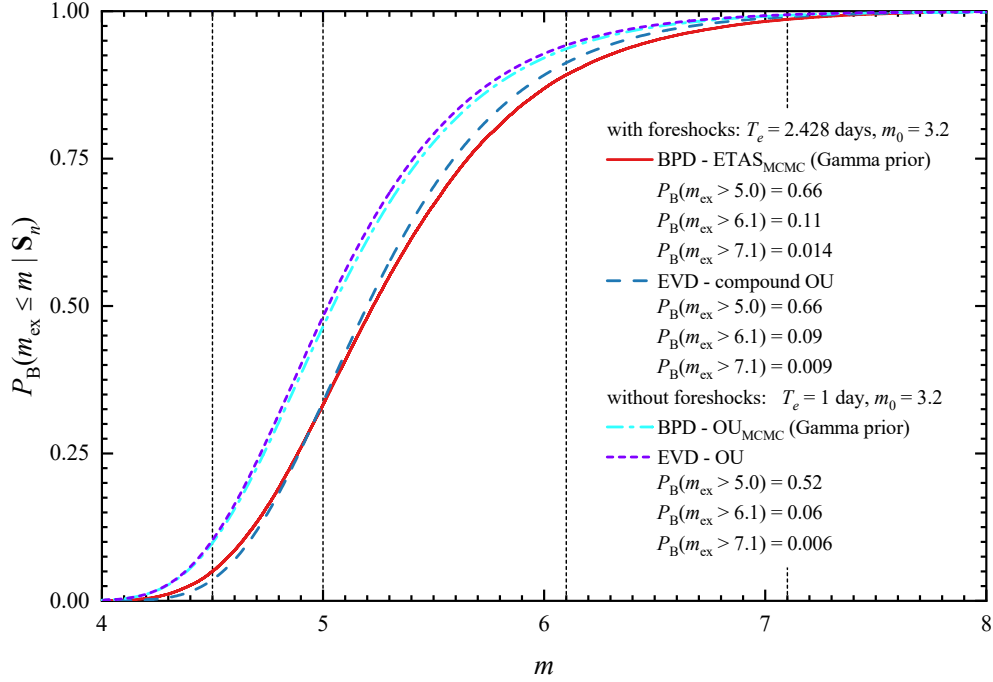


Figure 7. The extreme value and the Bayesian predictive distributions for the 2019 Ridgecrest sequence. The BPD is shown as a solid red curve using the ETAS model and MCMC sampling with the Gamma prior for the foreshocks and 1 day of aftershocks after the M7.1 mainshock. For the same sequence of events, the EVD using the compound OU law is shown as a dashed blue curve. For the rest of the distributions, 1 day of aftershocks after the M7.1 mainshock was used: the OU rate using the MCMC sampling with the Gamma prior (dash-dotted cyan curve); the Gumbel distribution with OU rate (short dashed violet curve).

424 the OU model parameters computed from the MCMC chain is illustrated in Figure S4.
 425 The matrix plot of the pairs of the OU model parameters is given in Figure S5. The val-
 426 ues for the mean and variance of the prior distribution (Gamma) of the OU model pa-
 427 rameters are provided in Table S1.

428 To investigate the influence of the foreshocks on the computation of the probabil-
 429 ities for the largest expected aftershocks, the EVD (8) using the compound OU law (5)
 430 and the BPD using the ETAS model (6) were computed for the earthquake sequence start-
 431 ing from the occurrence of the first M3.98 foreshock on 2019/07/04 (17:02:55 UTC). The
 432 earthquakes above magnitude $m \geq 3.2$ were used. In case of the BPD with the ETAS
 433 model, the target time interval $[T_s, T_e] = [0.03, 2.428]$ days was used with $T_0 = 0$ cor-
 434 responding to 2019/07/04 (17:02:55 UTC), which included the foreshocks and one day
 435 of aftershocks after the M7.1 mainshock. The values for the mean and variance of the
 436 prior distribution (Gamma) of the compound OU and ETAS model parameters are pro-
 437 vided in Tables S2-S3. The resulting BPD is plotted as a solid red curve in Figure 7. The
 438 probabilities of having the largest expected earthquakes during the next $\Delta T = 7$ days
 439 are provided in the legend. For the same sequence, the EVD (8) with the compound OU
 440 law (10) was computed and the corresponding probabilities to have the largest aftershocks
 441 during the next $\Delta T = 7$ days were estimated. This is plotted as a dashed blue curve
 442 in Figure 7. The MCMC sampling steps are given in Figure S6. The distribution of the
 443 compound OU model parameters computed from the MCMC chain is illustrated in Fig-
 444 ure S7. The matrix plot of the pairs of the compound OU model parameters is given in
 445 Figure S8.

446 The probabilities to have the largest expected earthquake above a certain magni-
 447 tude can be computed at specified times during the evolution of the sequence. This can
 448 be done by increasing progressively the upper limit T_e of the target time interval $[T_s, T_e]$
 449 for a fixed forecasting interval ΔT . Figure 8 illustrates the computed probabilities from
 450 the BPD (11) with the ETAS model (6) for the earthquake rate, and the exponential dis-
 451 tribution, Eq. (2), for the frequency-magnitude statistics. $T_0 = 0$ corresponded to the
 452 date 2019/07/04 (17:02:55 UTC) and $T_s = 0.03$ days. The MCMC sampling steps, the
 453 distribution of the ETAS model parameters, and the matrix plot of the pairs of the ETAS
 454 parameters are given in Figures S9-S11 for the following target time interval $[T_s, T_e] =$
 455 $[0.03, 2.4284]$ days. The probabilities were estimated for the largest expected earthquakes
 456 to be above $m_{ex} \geq 4.5, 5.0, 6.1, 6.4,$ and 7.1 . First, the probabilities were computed

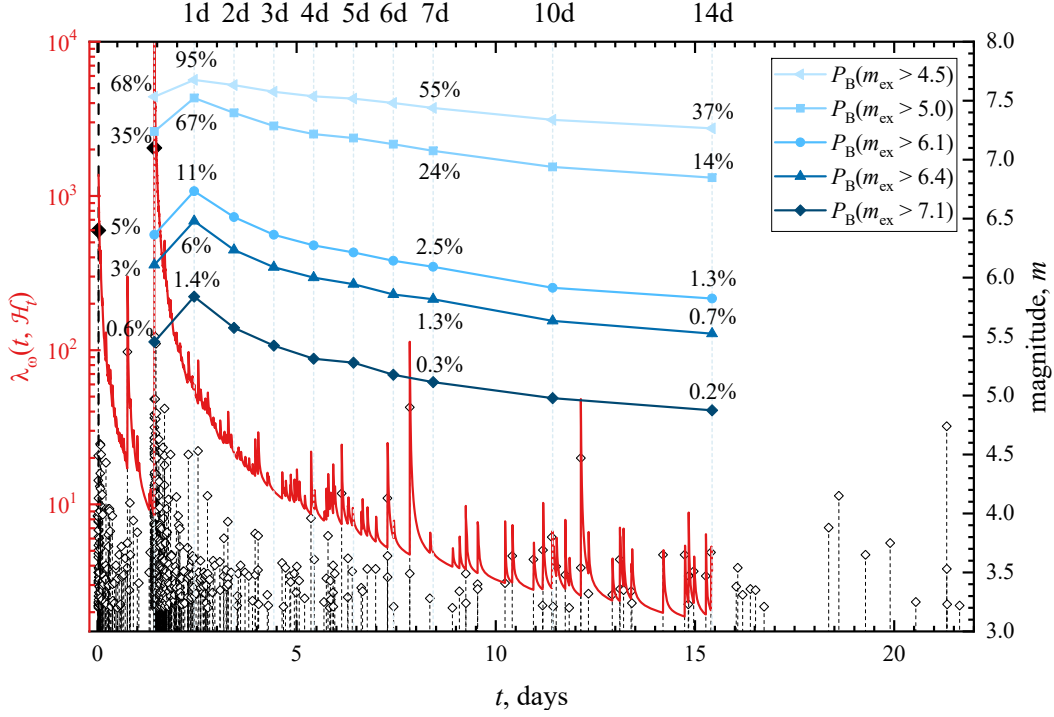


Figure 8. The probabilities for the largest expected earthquake to be above the magnitudes $m_{ex} \geq 4.5, 5.0, 6.1, 6.4, 7.1$ and during the progressively increasing time intervals since 2019/07/04 (17:02:55 UTC). The probabilities are estimated using the BPD combined with the ETAS model for the earthquake rate during the forecasting time interval $\Delta T = 7$ days and plotted in a logarithmic scale. The earthquake magnitudes of the 2019 Ridgecrest sequence are plotted as open diamonds for all events above magnitude $m \geq 3.2$. The fit of the ETAS model is shown as a solid curve.

457 using only the foreshock sequence right before the occurrence of the M7.1 mainshock with
 458 $T_e = 1.4284$ days. After that, the probabilities were recomputed for each subsequent
 459 day after the M7.1 mainshock by incorporating the information from the newly occurred
 460 aftershocks. For reference, the fit of the ETAS model is also shown as a red curve us-
 461 ing the following estimated model parameters $\{\beta, \mu, K, c, p, \alpha\} = \{2.39, 0.05, 3.47, 0.01, 1.35, 2.05\}$
 462 during the training time interval $[T_s, T_e] = [0.03, 15.4284]$ days. The forecast evolu-
 463 tion during 330 days after the occurrence of the M7.1 mainshock is given in Figure S12.
 464 It also illustrates the computed probabilities before the occurrence of the M5.5 event,
 465 which occurred on June 4, 2020.

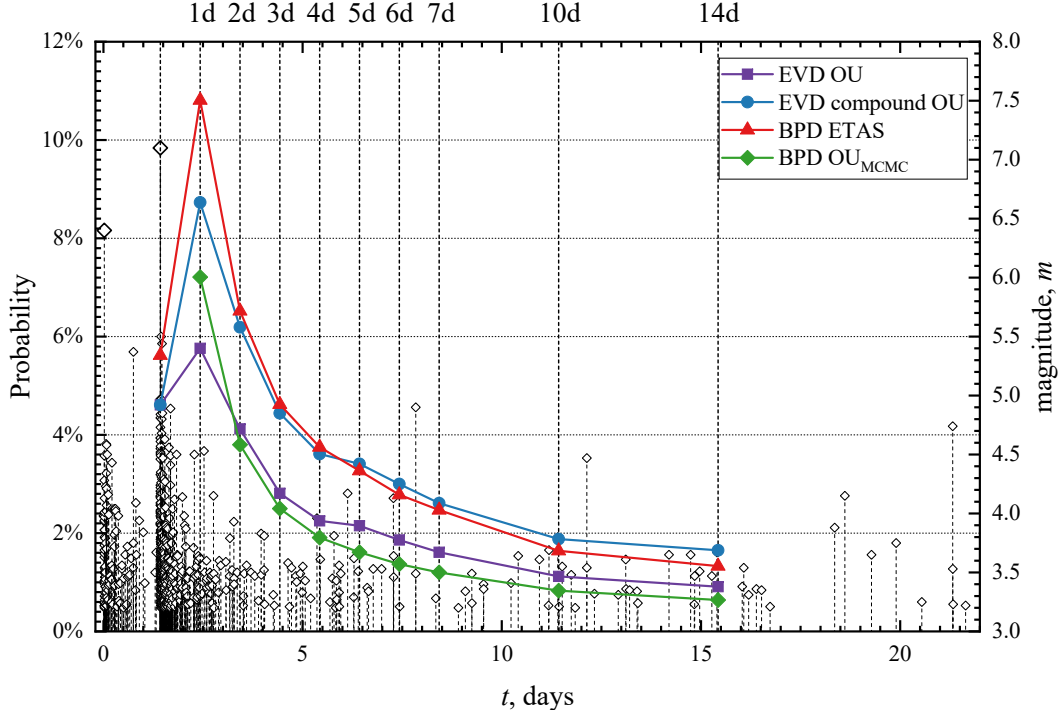


Figure 9. The comparison of the computed probabilities for the largest expected after-shock to be above magnitude $m_{\text{ex}} \geq 6.1$ during the progressively increasing time intervals since 2019/07/04 (17:02:55 UTC) for the fixed forecasting time interval $\Delta T = 7$ days. The four models were considered: the EVD with the OU law (solid squares), the EVD with the compound OU formula (solid circles), the BPD with the ETAS model (solid triangles), and the BPD with the OU law (solid diamonds).

466 Finally, Figure 9 provides a comparison of the results for the computation of the
 467 probabilities to have the expected largest aftershock to be greater than $m_{\text{ex}} \geq 6.1$ af-
 468 ter progressively increasing times T_e during the evolution of the sequence by using sev-
 469 eral methods examined in this work. The forecasting time interval was set to $\Delta T = 7$
 470 days. Specifically, the EVD with the OU law, Eqs. (8) and (9), was used and the esti-
 471 mated probabilities are plotted as solid squares. Next, the compound OU law (10) was
 472 used in the EVD computation and the results are plotted as solid circles. The computed
 473 probabilities from the BPD (11) with the ETAS model (6) as the earthquake rate are
 474 plotted as solid triangles. Finally, the probabilities were computed from the BPD with
 475 the earthquake rate modelled using the standard OU law (4) and are plotted as solid di-
 476 amonds.

4 Forecast Validation

The extreme value distribution, Eq. (8), and the Bayesian predictive distribution, Eq. (11), allow to compute the probability of having the expected largest event during the forecasting time interval ΔT . This computation critically depends on the proper simulation of the earthquake rate and the frequency-magnitude distribution of earthquakes during ΔT . Therefore, it is important to perform specific statistical tests to validate retrospectively as to how the models, that are used to describe those aspects of seismicity, accurately reproduce the observed earthquakes during the forecasting time intervals. One such test has been developed for the CSEP testing framework and is known as the N-test (Kagan & Jackson, 1995; Schorlemmer et al., 2007; Zechar et al., 2010). This test is used to quantify as to how accurately a given stochastic process reproduces the observed number of earthquakes above a certain magnitude during the forecasting time interval.

The following implementation of the N-test is considered in this work. It is assumed that N_{obs} earthquakes above magnitude m_0 occurred during a given forecasting time interval $[T_e, T_e + \Delta T]$. The posterior distribution of the parameters of a given stochastic point process model is sampled by the MCMC method N_{sim} times using the information of the earthquakes that occurred during the training time interval $[T_s, T_e]$. The MCMC sets of the model parameters are used to model forward in time a given point process during the forecasting time interval ΔT . The synthetic simulations produce the distribution of the number of the forecasted events at the end of the interval ΔT corresponding to each MCMC set of model parameters. The N-test statistically assesses whether the observed number of earthquakes N_{obs} is consistent with the forecast. The two quantile scores are computed (Zechar et al., 2010):

$$\delta_1 = 1 - P(N_{\text{obs}} - 1 | N_{\text{fore}}) , \quad (12)$$

$$\delta_2 = P(N_{\text{obs}} | N_{\text{fore}}) , \quad (13)$$

where N_{fore} is the average number of forecasted events above magnitude m_0 at the end of the forecasted time interval $T_e + \Delta T$. $P(x|\lambda)$ is the cumulative Poisson distribution with the expectation λ . As a result, δ_1 gives the probability of observing at least N_{obs} events and δ_2 gives the probability of observing at most N_{obs} events. The forecast underpredicts the observations if δ_1 is very small and the forecast overpredicts the observation if δ_2 is very small. Therefore, one can consider a one-sided test with an effective

507 significance level α_{eff} . If the computed probabilities δ_1 and δ_2 are smaller than α_{eff} then
 508 the forecast can be rejected.

509 The second test, which is known as M-test, has been suggested to check whether
 510 the distribution of the forecasted magnitudes is consistent with the observed magnitudes
 511 (Schorlemmer et al., 2007; Zechar et al., 2010). The M-test is performed by computing
 512 a quantile score κ . The values of κ below a significance level α_{eff} signify that the distri-
 513 bution of forecasted earthquake magnitudes is inconsistent with observations. The de-
 514 tails of computing the κ score can be found in Zechar et al. (2010).

515 Two more tests have been introduced to compare the performance of different fore-
 516 casting models. These are known as R-test and T-test (Schorlemmer et al., 2007; Rhoades
 517 et al., 2011). The R-test is performed by computing the log-likelihood ratio for two mod-
 518 els under consideration. The joint log-likelihood for given earthquake observations dur-
 519 ing the forecasting time interval can be written as follows:

$$L(\mathbf{M}|\mathbf{\Lambda}) = \log [\Pr(\mathbf{M}|\mathbf{\Lambda})] = \sum_{i \in \mathbf{B}} \{-\lambda(i) + m(i) \log[\lambda(i)] - \log[m(i)!]\}, \quad (14)$$

520 where $\mathbf{M} = \{m(i)|i \in \mathbf{B}\}$ is the set of the number of earthquakes $m(i)$ in each mag-
 521 nitude bin above a certain magnitude threshold. $\mathbf{\Lambda} = \{\lambda(i)|i \in \mathbf{B}\}$ is the earthquake
 522 forecast produced by a given point process in each magnitude bin, where $\lambda(i)$ is the num-
 523 ber of earthquakes forecasted in bin i and the magnitude binning coincides with the bin-
 524 ning of the earthquake catalog. In the definition of the joint log-likelihood, Eq. (14), it
 525 is assumed that the number of earthquakes in a forecast bin follows a Poisson distribu-
 526 tion: $\Pr(m|\lambda) = \frac{\lambda^m}{m!} \exp(-\lambda)$. To compare two models, $\mathbf{\Lambda}^1$ and $\mathbf{\Lambda}^2$, that forecast the
 527 same sequence of events one can compute the log-likelihood ratio: $R^{21} = L(\mathbf{M}|\mathbf{\Lambda}^2) -$
 528 $L(\mathbf{M}|\mathbf{\Lambda}^1)$.

529 In applying the R-test, one of the two models is assumed to be correct and is used
 530 to simulate the ensemble of synthetic earthquake events and compute the log-likelihood
 531 ratios for each synthetic record by using both models. These ratios are compared with
 532 the log-likelihood ratio computed for the observed earthquake sequence during the fore-
 533 casting interval. The properly normalized fraction of the simulated ratios that are less
 534 than the observed ratio gives the quantile score α (Schorlemmer et al., 2007). The val-
 535 ues of α , that are larger than a certain significance level, support the model that was as-
 536 sumed to be correct. This test is symmetric with respect to both models and can result
 537 in the situations when both models reject each other (Rhoades et al., 2011). To over-

538 come this difficulty, a so called T-test was introduced along with the sample informa-
 539 tion gain per earthquake (Rhoades et al., 2011). The sample information gain per earth-
 540 quake of the model Λ^2 over the model Λ^1 is defined as $I_N(\Lambda^2, \Lambda^1) = R^{21}/N_{\text{obs}}$, where
 541 N_{obs} is the number of observed earthquakes during the forecasting time interval ΔT . The
 542 T-test checks whether the sample information gain is statistically different from zero that
 543 indicates a significant difference between the two models (Rhoades et al., 2011).

544 One important difference in performing the above tests is implemented in this work.
 545 To account for the stochastic variability of the model parameters and the uncertainty
 546 associated with the prior information on the model parameters, the MCMC sampling
 547 of the posterior distribution of the model parameters is performed to produce a chain
 548 of model parameters that are used when simulating the models forward in time during
 549 the forecasting time interval.

550 The N-, M-, R-, and T-tests check the consistency of the underlying earthquake
 551 rate and frequency-magnitude distribution models. To test the consistency of the Bayesian
 552 predictive distribution, Eq. (11), with the observed largest earthquakes during the fore-
 553 casting time interval $[T_e, T_e + \Delta T]$, one can evaluate the posterior predictive p -value
 554 (Gelman et al., 2013, p.146). The Bayesian p_B -value gives the probability that the largest
 555 simulated earthquakes can be more extreme than the observed largest earthquake dur-
 556 ing the forecasting time interval. It is defined as follows:

$$p_B = \Pr [T(\hat{y}, \theta, \omega) \geq T(y, \theta, \omega) | y] , \quad (15)$$

557 where $T(y, \theta, \omega)$ is a *test quantity* computed for an observed variable y and simulated
 558 variable \hat{y} . The test quantity $T(y, \theta, \omega)$ characterizes data y with given model param-
 559 eters θ and ω . It is used for model checking in Bayesian analysis similar to a test statis-
 560 tic in classical testing. One possible choice for the test quantity is: $T(y, \theta, \omega) = \max(y)$.
 561 In practice, the Bayesian p_B -value can be computed from the MCMC chain of the model
 562 parameters θ and ω . For each set of the model parameters, the stochastic forecasting model
 563 is simulated forward in time and the largest event is extracted. This will allow to com-
 564 pute $T(\hat{y}, \theta, \omega) = \max(\hat{y})$. The realized test quantity $T(y, \theta, \omega) = \max(y)$ is simply
 565 the value of the largest observed earthquake during the forecasting time interval. There-
 566 fore, the estimated p_B -value is the proportion of the test quantities for the simulated max-
 567 imum events that are larger than the observed largest event:

$$p_B = \frac{|\{T(\hat{y}, \theta_i, \omega_i) \geq T(y) | i = 1, \dots, N_{\text{sim}}\}|}{N_{\text{sim}}} , \quad (16)$$

568 where N_{sim} is the total number of simulated sequences from the MCMC chain and $|x|$
 569 gives the size of the set x .

570 **4.1 Application to the 2019 Ridgecrest sequence**

571 The three point process models (OU, compound OU, and ETAS) were examined
 572 to see whether they were consistent with the observed seismicity during the forecasting
 573 time intervals $[T_e, T_e + \Delta T]$. For this, N- and M-tests were performed. Figure 10a shows
 574 the observed number of earthquakes above magnitude $m \geq 3.2$ (as solid black diamonds)
 575 during a fixed forecasting time interval $\Delta T = 7$ days and varying training time inter-
 576 val $[T_s, T_e]$. The numbers are plotted at the end of the forecasting time interval with the
 577 training interval ending after 1, 2, 3, 4, 5, 6, 7, 10, 14, 30 days after the M7.1 mainshock
 578 (the corresponding $T_e = 2.4284, 3.4284, \dots, 22.4284, 31.4284$). For example, the first
 579 symbol at $T_e + \Delta T = 9.4284$ days gives 89 earthquakes above magnitude 3.2 that oc-
 580 curred during 7 days starting after 1 day ($T_e = 2.4284$) after the M7.1 mainshock. It
 581 also shows the average forecasted numbers of earthquakes with the corresponding 95%
 582 bands (plotted as shaded regions) simulated by the three models. Each model was sim-
 583 ulated $N_{\text{sim}} = 100,000$ times forward in time during $\Delta T = 7$ days and for the vary-
 584 ing ends of the training time interval T_e . For each model simulation, the parameters were
 585 chosen from the MCMC chain obtained by sampling the posterior distribution of the model
 586 parameters. This allowed to incorporate the variability of the model parameters into the
 587 forecasted numbers. Similarly, Figure 10b illustrates the observed and forecasted num-
 588 ber of earthquakes when the end of the training time interval was held fixed at $T_e = 3.4284$
 589 days (2 days after the M7.1 mainshock) and the forecasting time interval varied $\Delta T =$
 590 1, 2, 5, 7, 10, 14 days. For the compound OU and ETAS models the preceding foreshock
 591 sequence was used. For the OU model only the aftershocks of the M7.1 mainshock were
 592 used.

593 To analyze to what extent the considered models underpredicted or overpredicted
 594 the observed sequence of earthquakes, the N-test was performed. The quantile scores com-
 595 puted during the N-test corresponding to the forecasting of the number of earthquakes
 596 are illustrated in Figure 11ab. Two threshold quantiles are plotted at 0.025 and 0.05 lev-
 597 els. δ_1 and δ_2 scores, Equations (12) and (13), were computed and plotted for the three
 598 models for the same forecasting time intervals of duration $\Delta T = 7$ days as used in Fig-
 599 ure 10a. In addition, the results of the M-test for the three models and for the same fore-

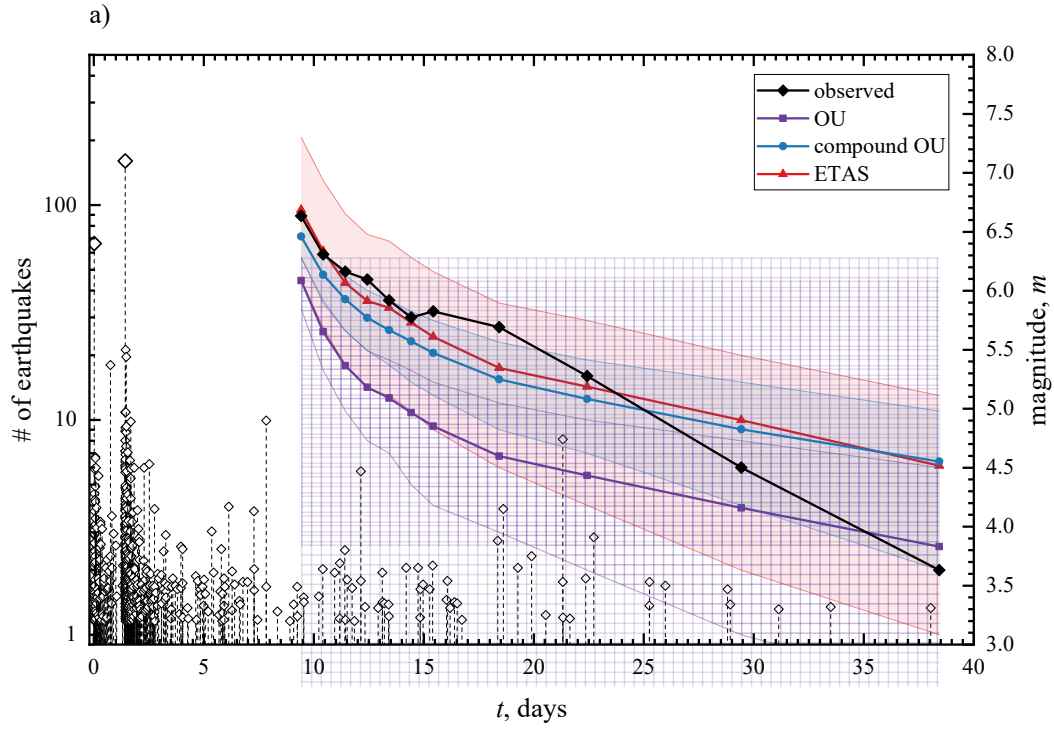


Figure 10. The observed and forecasted numbers of earthquakes starting after one day of aftershocks post M7.1 mainshock and during specified forecasting and training time intervals by using the three rate models: Omori-Utsu (OU), compound OU, and ETAS. a) The forecasting time interval $\Delta T = 7$ days is fixed while the end of the training time interval T_e is progressively increasing as $T_e = 2.428, 3.428, \dots, 22.428, 31.428$ days. The symbols indicate the number of the observed (black solid diamonds) and the mean number of forecasted earthquakes during $\Delta T = 7$ days computed at times $T_e + \Delta T$. b) The end of the training time interval is fixed at $T_e = 3.428$ days while the forecasting time interval is increasing as $\Delta T = 1, 2, 5, 7, 10, 14$. The shaded bands correspond to 95% confidence intervals.

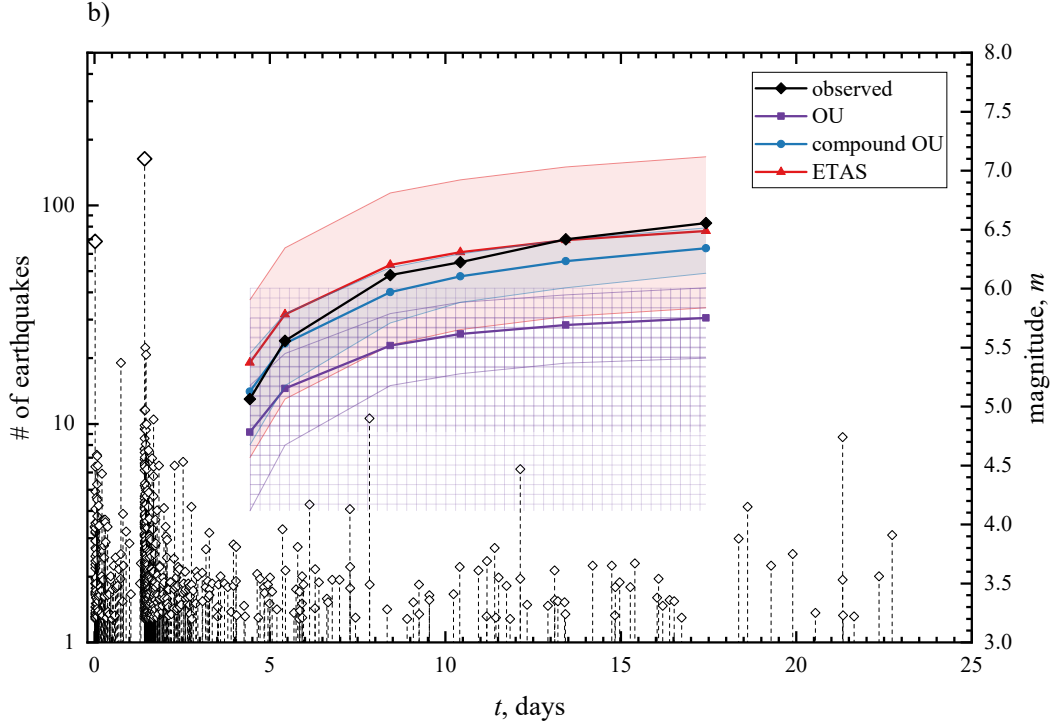


Figure 10. Continued.

600 casting time intervals are plotted in Figure 11c, where the quantile score κ character-
 601 izes the consistency of the forecasted earthquake magnitudes compared to the observed
 602 ones in each forecasting time interval. The quantile scores in a case of the varying fore-
 603 casting time interval $\Delta T = 1, 2, 5, 7, 10, 14$ days and fixed training time interval $T_e =$
 604 3.4284 days are given in Figure S13.

605 The models were also compared among each other by applying the R- and T-tests.
 606 Two pairs of the models were considered, i.e. the forecasts produced by the ETAS model
 607 versus the model with the OU law and the ETAS model versus the model with the comp-
 608 ound OU law. The results of the quantile score α for the R-test are plotted in Figure 12.
 609 The scores α were computed at the end of each forecasting time interval of duration ΔT
 610 as in Figure 10a. The corresponding sample information gain $I_N(\Lambda^2, \Lambda^1)$ for each pair
 611 of the models is given in Figure 13. The quantile score α and the information gain per
 612 earthquake in a case of the varying forecasting time interval $\Delta T = 1, 2, 5, 7, 10, 14$ days
 613 and fixed training time interval $T_e = 3.4284$ days are given in Figures S14 and S15. In
 614 both pairs of models, it was assumed that the ETAS model (with the forecast Λ^2) is the

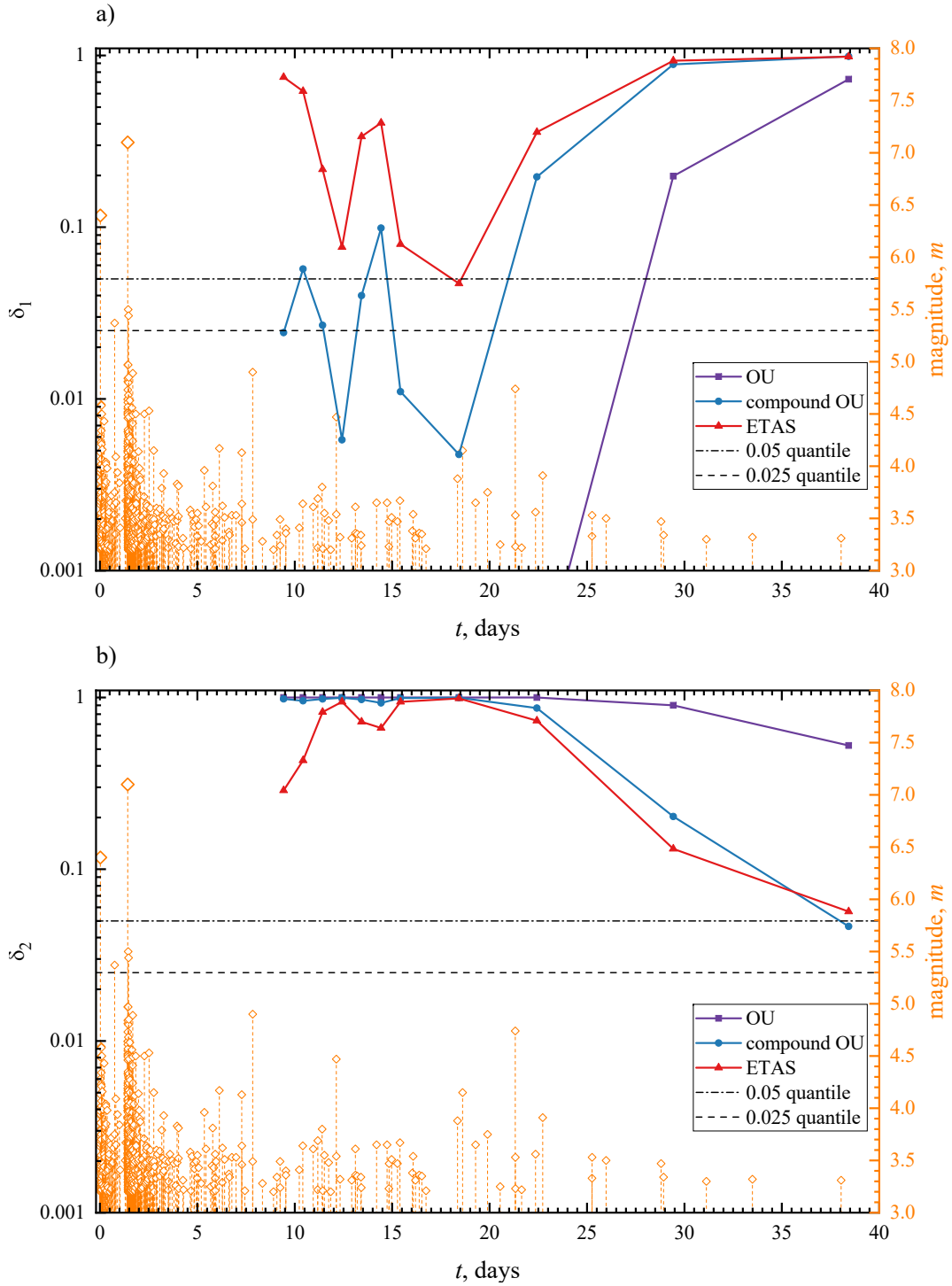


Figure 11. Plot of the quantile scores a) δ_1 (N-test), b) δ_2 (N-test), and c) κ (M-test) for the performance of the aftershock forecasts based on the three point process models. The scores are computed at the end of each forecasting time interval of fixed duration $\Delta T = 7$ days and varying training time intervals $[T_s, T_e]$ as in Figure 10.

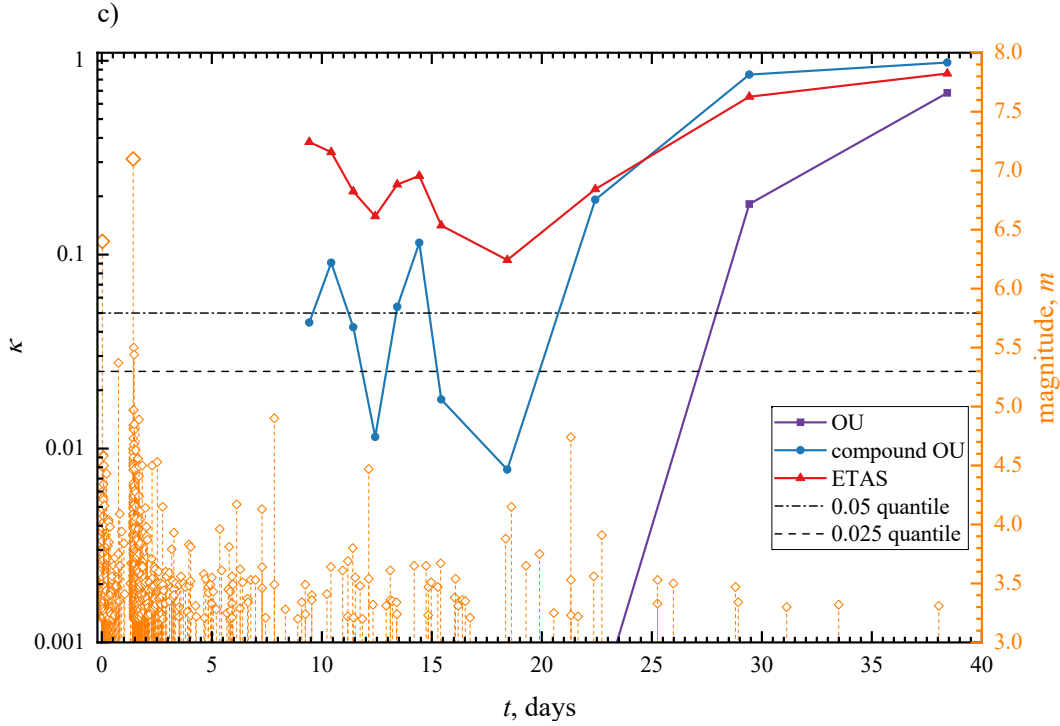


Figure 11. Continued.

615 correct model to simulate the synthetic sequences of events during the forecasting time
 616 intervals.

617 Finally, the Bayesian p_B -value, Eq. (16), was computed for the three models. This
 618 is plotted in Figure 14 for the varying training time intervals. Figure S16 illustrates the
 619 dependency of the p_B -value on the varying forecasting time interval as in Figure S14.

620 5 Discussion

621 The 2019 Ridgecrest earthquake sequence occurred in a complex network of fault
 622 structures. It generated a prominent foreshock sequence that culminated in the occur-
 623 rence of the M7.1 mainshock, which was followed by a productive aftershock sequence.
 624 This complexity of the sequence was partially reflected in the frequency-magnitude statis-
 625 tics of foreshocks and aftershocks. It also manifested in the clustering of earthquakes in
 626 time and in space. The complex pattern of multi-segmented ruptures of the two strongest
 627 events in the sequence contributed to the assumed stress transfer pattern, which affected
 628 the distribution of subsequent triggered aftershocks.

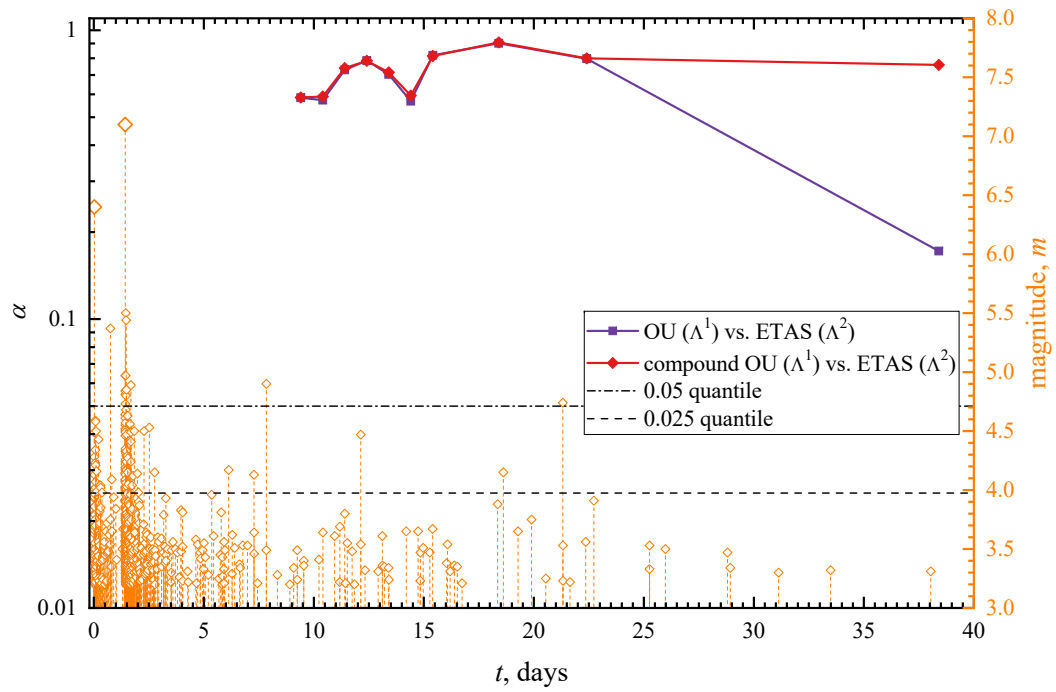


Figure 12. Plot of the quantile score α (R-test) for the comparative test of the ETAS model versus the forecast based on the OU model and on the compound OU model. The scores are computed at the end of each forecasting time interval as in Figure 11.

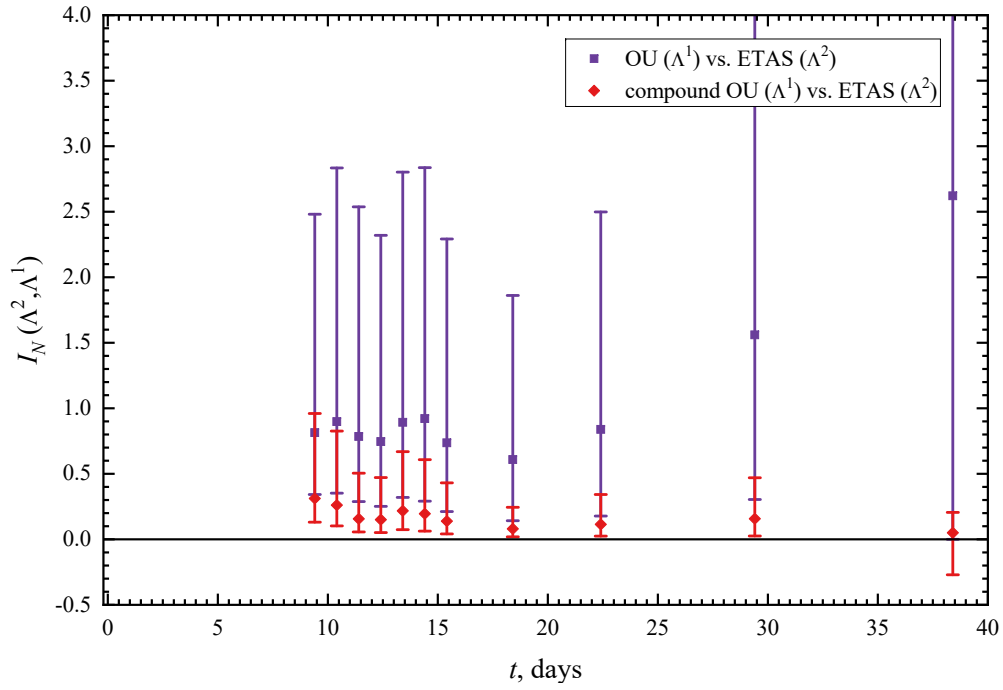


Figure 13. The sample information gain for the pairs of the models. The solid squares correspond to the comparison of the forecasts based on the ETAS model versus the forecasts based on the OU model. The solid diamonds correspond to the comparison of the forecasts based on the ETAS model versus the forecast based on the compound OU model. The 95% confidence intervals are given.

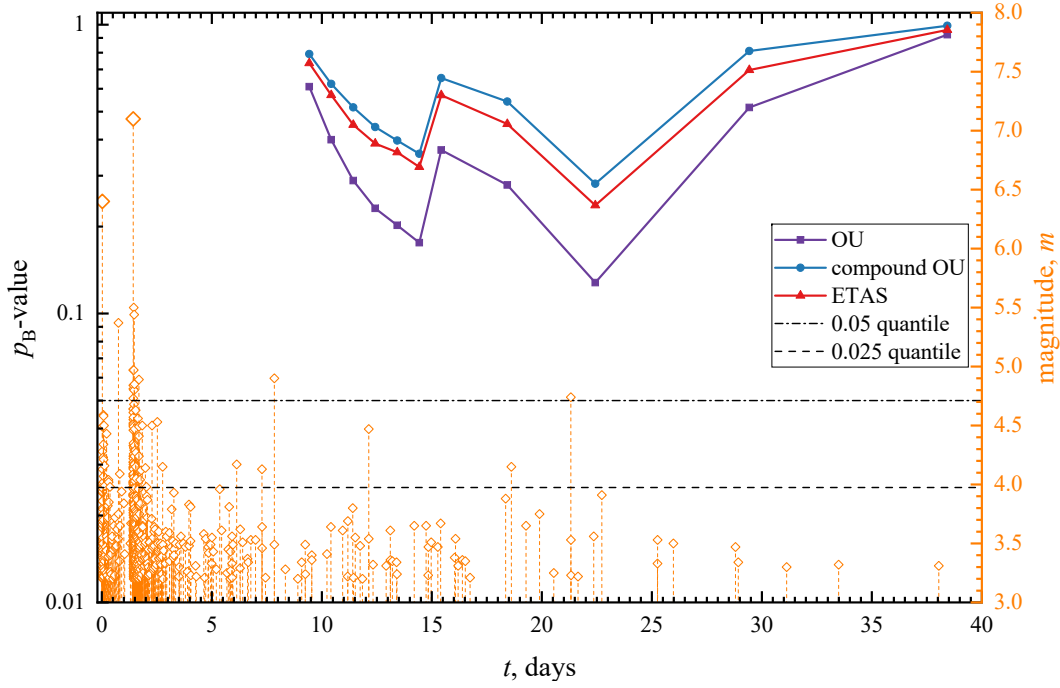


Figure 14. Plot of the Bayesian predictive distribution p_B -value for the three models. The p_B -values are computed at the end of each forecasting time interval as in Figure 11.

629 One of the main objectives of this work was to provide a framework to compute
 630 the probabilities for the occurrence of the largest expected aftershocks during different
 631 stages of the evolution of this sequence by incorporating the preceding seismicity. This
 632 was accomplished through two main approaches. The first one was based on the assump-
 633 tion that the occurrence of earthquakes could be modelled as a non-homogenous Pois-
 634 son process with a specified parametric model for the earthquake rate and the frequency-
 635 magnitude distribution. Specifically, one can use the OU law (4) or the compound OU
 636 law (5) and the exponential distribution for the earthquake magnitudes, Eq. (2). Then,
 637 the probabilities can be estimated from the EVD (8) for a specific forecasting time in-
 638 terval ΔT by using the point estimates of the model parameters. The second approach
 639 employed the computation of the BPD (11), which allowed to incorporate the uncertain-
 640 ties of the model parameters into the computation of the corresponding probabilities.
 641 This approach also requires to provide certain *a priori* knowledge on the model param-
 642 eters specified through the prior distributions.

643 The comparison of these two approaches with the combination of the three mod-
644 els for the earthquake rate and either including or excluding the foreshocks is illustrated
645 in Figure 7. The results clearly illustrate that the inclusion of the foreshocks along with
646 the earthquake rate models that favour earthquake clustering produces higher probabilit-
647 ities for the occurrence of the largest expected earthquakes during the specified forecast-
648 ing period of $\Delta T = 7$ days.

649 It is interesting to note, the 2019 Ridgecrest earthquake sequence bears a striking
650 similarity to the 2016 Kumamoto, Japan, earthquake sequence. Both sequences had a
651 pronounced foreshock sequence which was triggered by the strong foreshocks of similar
652 magnitudes (M6.4 vs. M6.5) and duration. They occurred on the different fault segments
653 than the mainshock fault rupture. The b -values of the GR relation and p values of the
654 OU law were also smaller than the values for the aftershocks generated by the mainshocks.
655 The mainshock magnitudes were also similar (M7.1 vs. M7.3) and had the strike-slip mech-
656 anisms. It is difficult to pin point the common stress conditions and state of faults that
657 lead to the occurrence of both sequences but some clues may be inferred from the seis-
658 micity patterns that preceded and followed both events and can be related to the changes
659 in the stress field (Nanjo et al., 2019; Nanjo, 2020).

660 To validate the three stochastic models, several statistical tests (N-, M-, R-, and
661 T-tests) were applied retrospectively for several combinations of the training and fore-
662 casting time intervals. The results of the N-test indicate that the OU model underes-
663 timated the observed number of earthquakes for most of the forecasting time intervals.
664 The compound OU model performed better especially in the early stages of the evolu-
665 tion of the sequence. The ETAS model approximated the observed number of earthquakes
666 during the all considered forecasting time intervals, however, the ETAS model also had
667 wider 95% spread in the number of forecasted earthquakes (Figure 10). This is the con-
668 sequence of the branching nature of the ETAS process and the deviation of the distri-
669 bution of the number of events from the Poisson distribution. The ETAS model was also
670 consistent in reproducing the distribution of the magnitudes in each bin that is illustrated
671 in Figure 11c through the κ quantile score of the M-test.

672 The comparative analysis of the ETAS model versus the OU and the compound
673 OU models also confirmed that the forecast based on the ETAS model outperformed the
674 forecasts based on the other two models. This is illustrated in Figure 12, where the quan-

675 tile score α from the R-test is plotted at the end of each forecasting time interval. The
 676 values of the score above the threshold level 0.025 indicate that the ETAS model out-
 677 performed the other two models. The similar conclusion is drawn from the plot (Figure 13)
 678 of the sample information gain $I_N(\mathbf{\Lambda}^2, \mathbf{\Lambda}^1)$. The results of the T-test confirmed that the
 679 ETAS model provided a statistically significant information gain with respect to the mod-
 680 els based on the OU or compound OU rates except for the last forecasting interval end-
 681 ing at 38.4284 days, where the ETAS model and the model based on the compound OU
 682 rate performed similarly. For the last forecasting time interval ending at $T_e + \Delta T =$
 683 38.4284 days, there were only three events above magnitude $m \geq 3.2$. The compound
 684 OU model produced relatively close results when computing the probabilities for the oc-
 685 currence of the largest expected earthquakes (Figure 9).

686 One limitation of the above tests (M-, R-, T-) based on the computing of the joint
 687 log-likelihoods, Eq. (14), is that they assume that the distribution of the number of earth-
 688 quakes in the forecasting time interval is Poisson. This is true for the both point pro-
 689 cess models based on the OU law. However, the ETAS model deviates from the Pois-
 690 son assumption. This was already demonstrated in Shcherbakov et al. (2019) when com-
 691 puting the Bayesian predictive distribution. Therefore, the application of these tests to
 692 the ETAS based models has to be considered approximate.

693 The above tests implemented in this work used the MCMC sampling of the pos-
 694 terior distribution of the model parameters. This allowed to incorporate the stochastic
 695 variability of the model parameters and the uncertainties associated with the prior in-
 696 formation on the model parameters into the computation of the resulting probabilities
 697 and when performing the statistical tests. The consistency of the Bayesian predictive dis-
 698 tribution was evaluated by estimating the Bayesian p_B -value, Eq. (16). The values of p_B
 699 within a reasonable range (say [0.05, 0.95]) indicate that a model is expected to repro-
 700 duce a specific aspect of the data given by the test quantity $T(y)$. Whereas, the values
 701 close to 0 or 1 signify that this aspect of the data is not captured by the model. All the
 702 three models were consistent in reproducing the observed largest earthquakes in each fore-
 703 casting time interval.

704 The analysis of the 2019 Ridgecrest earthquake sequence showed that the Bayesian
 705 predictive framework combined with the ETAS model outperformed more traditional ap-
 706 proaches based on the Omori-Utsu type models when using the extreme value distribu-

707 tion to compute the probabilities for the occurrence of the largest events. The latter ap-
 708 proach uses point estimates of the model parameters to compute the corresponding prob-
 709 abilities. However, large uncertainties associated with these model parameters can re-
 710 sult in significant underestimation/overestimation of the probabilities for the largest ex-
 711 pected events or the numbers of earthquakes above a certain magnitude during the fore-
 712 casting time intervals. This is particularly evident for the Omori-Utsu law, where the
 713 productivity of the process is controlled by the K_o parameter, which is typically estimated
 714 with large uncertainties (Marsan & Helmstetter, 2017; Shebalin et al., 2020). On the other
 715 hand, the Bayesian framework fully incorporates these model uncertainties into the com-
 716 putation of the probabilities. It also allows to account for the correlations among the model
 717 parameters. In addition, the Bayesian approach provides a flexible way of separating those
 718 uncertainties into epistemic and aleatory types (Kiureghian & Ditlevsen, 2009; Gersten-
 719 berger et al., 2020). It allows to control the epistemic uncertainties through the prior in-
 720 formation of the model parameters and incorporates the aleatory variability of the stochas-
 721 tic process through the earthquake rate models and the frequency-magnitude distribu-
 722 tions.

723 6 Conclusions

724 The 2019 Ridgecrest earthquake sequence was characterized by the complex clus-
 725 tering of seismicity with earthquakes occurring on a distributed fault network. It also
 726 presented a good opportunity to analyze the sequence retrospectively in order to test sev-
 727 eral statistical approaches to study the sequence in temporal and magnitude domains
 728 and to forecast the occurrence of the largest expected aftershocks during the evolution
 729 of the sequence.

730 Two approaches were used to compute the probabilities of having the largest ex-
 731 pected earthquakes to be above certain magnitudes after specified time intervals and dur-
 732 ing the fixed forecasting time interval $\Delta T = 7$ days. For the first approach, the EVD (8)
 733 with the OU law (4) or the compound OU formula (5) was used. In the second approach,
 734 the Bayesian predictive distribution, Eq. (11), combined with the OU law or the ETAS
 735 model (6) was used. The comparison of these approaches are illustrated in Figure 9.

736 Applying these two approaches to the 2019 Ridgecrest earthquake sequence revealed
 737 that the incorporation of the foreshock sequence for the subsequent computation of the

738 probabilities to have the largest expected aftershocks above a certain magnitude was im-
739 portant. This was also relevant to the choice of the model to approximate the earthquake
740 rate. Specifically, the compound OU law (5) and the ETAS model (6) provided a bet-
741 ter approximation for the earthquake rate than the OU law (4) applied separately to the
742 foreshock and aftershock sequences during the forecasting time intervals. These conclu-
743 sions have been verified by several statistical tests. In addition, a new test based on the
744 Bayesian p_B -value was implemented and applied to check the consistency of the Bayesian
745 predictive distribution. Overall, the ETAS model passed the tests most of the time and
746 was successful in reproducing the observed number of earthquakes and the distribution
747 of magnitudes. As a result, the computed probabilities using the Bayesian predictive dis-
748 tribution (Figure 8) for the largest expected earthquake during the evolution of the 2019
749 Ridgecrest sequence can be considered accurate.

750 **Data and Resources**

751 The Southern California Seismic Network database, SCSN (2020), [https://service](https://service.scedc.caltech.edu/eq-catalogs/date_mag_loc.php)
752 [.scedc.caltech.edu/eq-catalogs/date_mag_loc.php](https://service.scedc.caltech.edu/eq-catalogs/date_mag_loc.php), was used to download the seis-
753 mic catalog (last accessed on December 1, 2020).

754 U.S. Geological Survey and California Geological Survey quaternary fault and fold
755 database for the United States , USGS (2006), was downloaded from the USGS web site:
756 <https://earthquake.usgs.gov/hazards/qfaults/> (last accessed on June 1, 2020).

757 The data analysis was performed using computer scripts written in Matlab and can
758 be requested from the author.

759 The Supporting Information for this article includes Tables S1-S3 with the param-
760 eters of the Gamma distribution, which was used as a prior distribution for the param-
761 eters of the three models considered in the work. It also includes plots illustrating the
762 fit of the compound OU (Figure S1) and the ETAS (Figure S2) models. The MCMC sam-
763 pling of the model parameters for the OU (Figures S4-S5), the compound OU (Figures S6-
764 8), the ETAS (Figures S9-S11) models are provided for one specific training and fore-
765 casting time intervals. The forecast evolution during 330 days after the occurrence of the
766 M7.1 mainshock is given in Figure S12. The additional quantile scores of the plots are
767 given in Figures S13-S16.

768 **Acknowledgments**

769 The constructive comments by two anonymous reviewers helped to improve the manuscript.

770 This work has been supported by the NSERC Discovery grant.

771 **References**

772 Barnhart, W. D., Hayes, G. P., & Gold, R. D. (2019). The July 2019 Ridgecrest,
773 California, earthquake sequence: Kinematics of slip and stressing in cross-fault
774 ruptures. *Geophys. Res. Lett.*, *46*, 11859-11867. doi: 10.1029/2019gl084741

775 Båth, M. (1965). Lateral inhomogeneities of the upper mantle. *Tectonophysics*, *2*,
776 483-514.

777 Bender, B. (1983). Maximum likelihood estimation of b values for magnitude
778 grouped data. *Bull. Seismol. Soc. Am.*, *73*(3), 831-851.

779 Campbell, K. W. (1982). Bayesian analysis of extreme earthquake occurrences. Part
780 I. Probabilistic hazard model. *Bull. Seismol. Soc. Am.*, *72*(5), 1689-1705.

781 Cattania, C., Werner, M. J., Marzocchi, W., Hainzl, S., Rhoades, D., Gerstenberger,
782 M., ... Jordan, T. H. (2018). The forecasting skill of physics-based seismicity
783 models during the 2010-2012 Canterbury, New Zealand, earthquake sequence.
784 *Seismol. Res. Lett.*, *89*(4), 1238-1250. doi: 10.1785/0220180033

785 Coles, S. (2001). *An Introduction to Statistical Modeling of Extreme Values*. London:
786 Springer.

787 Console, R., Lombardi, A. M., Murru, M., & Rhoades, D. (2003). Båth's law and
788 the self-similarity of earthquakes. *J. Geophys. Res.*, *108*(B2), 2128. doi: 10
789 .1029/2001JB001651

790 Daley, D. J., & Vere-Jones, D. (2003). *An Introduction to the Theory of Point Pro-*
791 *cesses* (2nd ed., Vol. 1). New York: Springer.

792 Ebrahimian, H., & Jalayer, F. (2017). Robust seismicity forecasting based on
793 Bayesian parameter estimation for epidemiological spatio-temporal aftershock
794 clustering models. *Sci. Rep.*, *7*, 9803. doi: 10.1038/s41598-017-09962-z

795 Ebrahimian, H., Jalayer, F., Asprone, D., Lombardi, A. M., Marzocchi, W., Prota,
796 A., & Manfredi, G. (2014). Adaptive daily forecasting of seismic aftershock
797 hazard. *Bull. Seismol. Soc. Am.*, *104*(1), 145-161. doi: 10.1785/0120130040

798 Felzer, K. R., Abercrombie, R. E., & Ekström, G. (2004). A common origin for
799 aftershocks, foreshocks, and multiplets. *Bull. Seismol. Soc. Am.*, *94*(1), 88-98.

- 800 doi: 10.1785/0120030069
- 801 Gelman, A., Carlin, J., Stern, H., Dunson, D., Vehtari, A., & Rubin, D. (2013).
802 *Bayesian Data Analysis* (3rd ed.). Boca Raton: CRC Press.
- 803 Gerstenberger, M. C., Marzocchi, W., Allen, T., Pagani, M., Adams, J., Danciu, L.,
804 ... Petersen, M. D. (2020). Probabilistic seismic hazard analysis at regional
805 and national scale: State of the art and future challenges. *Rev. Geophys.*,
806 *58*(2), e2019RG000653. doi: 10.1029/2019rg000653
- 807 Gerstenberger, M. C., Wiemer, S., Jones, L. M., & Reasenber, P. A. (2005). Real-
808 time forecasts of tomorrow's earthquakes in California. *Nature*, *435*(7040),
809 328-331. doi: 10.1038/Nature03622
- 810 Gutenberg, B., & Richter, C. F. (1944). Frequency of earthquakes in California.
811 *Bull. Seismol. Soc. Am.*, *4*, 185-188.
- 812 Hainzl, S. (2016a). Apparent triggering function of aftershocks resulting from rate-
813 dependent incompleteness of earthquake catalogs. *J. Geophys. Res.*, *121*(9),
814 6499-6509. doi: 10.1002/2016jb013319
- 815 Hainzl, S. (2016b). Rate-dependent incompleteness of earthquake catalogs. *Seismol.*
816 *Res. Lett.*, *87*(2), 337-344. doi: 10.1785/0220150211
- 817 Hardebeck, J. L. (2020). A stress-similarity triggering model for aftershocks of the
818 M_w 6.4 and 7.1 Ridgecrest earthquakes. *Bull. Seismol. Soc. Am.*, *110*(4), 1716-
819 1727. doi: 10.1785/0120200015
- 820 Hardebeck, J. L., Llenos, A. L., Michael, A. J., Page, M. T., & van der Elst, N.
821 (2019). Updated California aftershock parameters. *Seismol. Res. Lett.*, *90*(1),
822 262-270. doi: 10.1785/0220180240
- 823 Harte, D. (2010). PtProcess: An R package for modelling marked point process in-
824 dexed by time. *J. Stat. Softw.*, *35*(8), 1-32. doi: 10.18637/jss.v035.i08
- 825 Harte, D. (2017). Probability distribution of forecasts based on the ETAS model.
826 *Geophys. J. Int.*, *210*(1), 90-104. doi: 10.1093/gji/ggx146
- 827 Helmstetter, A., Kagan, Y. Y., & Jackson, D. D. (2006). Comparison of short-term
828 and time-independent earthquake forecast models for southern California. *Bull.*
829 *Seismol. Soc. Am.*, *96*(1), 90-106. doi: 10.1785/0120050067
- 830 Holschneider, M., Narteau, C., Shebalin, P., Peng, Z., & Schorlemmer, D. (2012).
831 Bayesian analysis of the modified Omori law. *J. Geophys. Res.*, *117*, B06317.
832 doi: 10.1029/2011jb009054

- 833 Kagan, Y. Y. (2004). Short-term properties of earthquake catalogs and models of
834 earthquake source. *Bull. Seismol. Soc. Am.*, *94*(4), 1207-1228.
- 835 Kagan, Y. Y., & Jackson, D. D. (1995). New seismic gap hypothesis: Five years af-
836 ter. *J. Geophys. Res.*, *100*(B3), 3943-3959. doi: 10.1029/94jb03014
- 837 Kiureghian, A. D., & Ditlevsen, O. (2009). Aleatory or epistemic? Does it matter?
838 *Struct. Safety*, *31*(2), 105-112. doi: 10.1016/j.strusafe.2008.06.020
- 839 Liu, C. L., Lay, T., Brodsky, E. E., Dascher-Cousineau, K., & Xiong, X. (2019).
840 Coseismic rupture process of the large 2019 Ridgecrest earthquakes from joint
841 inversion of geodetic and seismological observations. *Geophys. Res. Lett.*, *46*,
842 11820-11829. doi: 10.1029/2019gl084949
- 843 Mancini, S., Segou, M., Werner, M. J., & Parsons, T. (2020). The predictive skills of
844 elastic Coulomb rate-and-state aftershock forecasts during the 2019 Ridgecrest,
845 California, earthquake sequence. *Bull. Seismol. Soc. Am.*, *110*(4), 1736-1751.
846 doi: 10.1785/0120200028
- 847 Marsan, D., & Helmstetter, A. (2017). How variable is the number of triggered af-
848 tershocks? *J. Geophys. Res.*, *122*(7), 5544-5560. doi: 10.1002/2016jb013807
- 849 Michael, A. J., McBride, S. K., Hardebeck, J. L., Barall, M., Martinez, E., Page,
850 M. T., ... Wein, A. M. (2019). Statistical seismology and communication of
851 the USGS operational aftershock forecasts for the 30 November 2018 Mw \hat{A} 7.1
852 Anchorage, Alaska, earthquake. *Seismol. Res. Lett.*, *91*(1), 153-173. doi:
853 10.1785/0220190196
- 854 Milner, K. R., Field, E. H., Savran, W. H., Page, M. T., & Jordan, T. H. (2020).
855 Operational earthquake forecasting during the 2019 Ridgecrest, California,
856 earthquake sequence with the UCERF3-ETAS model. *Seismol. Res. Lett.*,
857 *91*(3), 1567-1578. doi: 10.1785/0220190294
- 858 Nanjo, K. Z. (2020). Were changes in stress state responsible for the 2019 Ridge-
859 crest, California, earthquakes? *Nat. Commun.*, *11*(1). doi: 10.1038/s41467-020
860 -16867-5
- 861 Nanjo, K. Z., Izutsu, J., Orihara, Y., Kamogawa, M., & Nagao, T. (2019). Changes
862 in seismicity pattern due to the 2016 Kumamoto earthquakes identify a highly
863 stressed area on the Hinagu fault zone. *Geophys. Res. Lett.*, *46*(16), 9489-9496.
864 doi: 10.1029/2019gl083463
- 865 Nanjo, K. Z., Tsuruoka, H., Yokoi, S., Ogata, Y., Falcone, G., Hirata, N., ...

- 866 Zhuang, J. (2012). Predictability study on the aftershock sequence follow-
867 ing the 2011 Tohoku-Oki, Japan, earthquake: first results. *Geophys. J. Int.*,
868 191(2), 653-658. doi: 10.1111/j.1365-246X.2012.05626.x
- 869 Ogata, Y. (1983). Estimation of the parameters in the modified Omori formula for
870 aftershock frequencies by the maximum-likelihood procedure. *J. Phys. Earth*,
871 31(2), 115-124. doi: 10.4294/jpe1952.31.115
- 872 Ogata, Y. (1988). Statistical-models for earthquake occurrences and residual analy-
873 sis for point-processes. *J. Am. Stat. Assoc.*, 83(401), 9-27.
- 874 Ogata, Y. (1999). Seismicity analysis through point-process modeling: A review.
875 *Pure Appl. Geophys.*, 155(2-4), 471-507. doi: 10.1007/s000240050275
- 876 Ogata, Y. (2017). Statistics of earthquake activity: Models and methods for earth-
877 quake predictability studies. *Annu. Rev. Earth Planet. Sci.*, 45, 497-527. doi:
878 10.1146/annurev-earth-063016-015918
- 879 Ogata, Y., & Omi, T. (2020). Statistical monitoring and early forecasting of
880 the earthquake sequence: Case studies after the 2019 M 6.4 Searles Valley
881 earthquake, California. *Bull. Seismol. Soc. Am.*, 110(4), 1781-1798. doi:
882 10.1785/0120200023
- 883 Omi, T., Ogata, Y., Hirata, Y., & Aihara, K. (2013). Forecasting large af-
884 tershocks within one day after the main shock. *Sci. Rep.*, 3, 2218. doi:
885 10.1038/srep02218
- 886 Omi, T., Ogata, Y., Hirata, Y., & Aihara, K. (2014). Estimating the ETAS model
887 from an early aftershock sequence. *Geophys. Res. Lett.*, 41(3), 850-857. doi: 10
888 .1002/2013gl058958
- 889 Omi, T., Ogata, Y., Shiomi, K., Enescu, B., Sawazaki, K., & Aihara, K. (2016). Au-
890 tomatic aftershock forecasting: A test using real-time seismicity data in Japan.
891 *Bull. Seismol. Soc. Am.*, 106(6), 2450-2458. doi: 10.1785/0120160100
- 892 Omi, T., Ogata, Y., Shiomi, K., Enescu, B., Sawazaki, K., & Aihara, K. (2019).
893 Implementation of a real-time system for automatic aftershock forecasting in
894 Japan. *Seismol. Res. Lett.*, 90, 242-250. doi: 10.1785/0220180213
- 895 Omori, F. (1894). On after-shocks of earthquakes. *J. Coll. Sci. Imp. Univ. Tokyo*, 7,
896 113-200.
- 897 Page, M. T., van der Elst, N., Hardebeck, J., Felzer, K., & Michael, A. J. (2016).
898 Three ingredients for improved global aftershock forecasts: Tectonic region,

- 899 time-dependent catalog incompleteness, and intersequence variability. *Bull.*
900 *Seismol. Soc. Am.*, 106(5), 2290-2301. doi: 10.1785/0120160073
- 901 Peng, Z. G., Vidale, J. E., & Houston, H. (2006). Anomalous early aftershock decay
902 rate of the 2004 Mw 6.0 Parkfield, California, earthquake. *Geophys. Res. Lett.*,
903 33(17), L17307. doi: 10.1029/2006GL026744
- 904 Reasenberg, P. A., & Jones, L. M. (1989). Earthquake hazard after a mainshock in
905 California. *Science*, 243(4895), 1173-1176. doi: 10.1126/science.243.4895.1173
- 906 Renard, B., Sun, X., & Lang, M. (2013). Bayesian methods for non-stationary ex-
907 treme value analysis. In A. AghaKouchak, D. Easterling, K. Hsu, S. Schubert,
908 & S. Sorooshian (Eds.), *Extremes in a Changing Climate: Detection, Analysis*
909 *and Uncertainty* (p. 39-95). Dordrecht: Springer.
- 910 Rhoades, D. A., Christophersen, A., Gerstenberger, M. C., Liukis, M., Silva, F.,
911 Marzocchi, W., ... Jordan, T. H. (2018). Highlights from the first ten years of
912 the New Zealand earthquake forecast testing center. *Seismol. Res. Lett.*, 89(4),
913 1229-1237. doi: 10.1785/0220180032
- 914 Rhoades, D. A., Liukis, M., Christophersen, A., & Gerstenberger, M. C. (2016).
915 Retrospective tests of hybrid operational earthquake forecasting models for
916 Canterbury. *Geophys. J. Int.*, 204(1), 440-456. doi: 10.1093/gji/ggv447
- 917 Rhoades, D. A., Schorlemmer, D., Gerstenberger, M. C., Christophersen, A., Zechar,
918 J. D., & Imoto, M. (2011). Efficient testing of earthquake forecasting models.
919 *Acta Geophys.*, 59(4), 728-747. doi: 10.2478/s11600-011-0013-5
- 920 Ross, Z. E., Idini, B., Jia, Z., Stephenson, O. L., Zhong, M. Y., Wang, X., ...
921 Jung, J. (2019). Hierarchical interlocked orthogonal faulting in the
922 2019 Ridgecrest earthquake sequence. *Science*, 366(6463), 346-351. doi:
923 10.1126/science.aaz0109
- 924 Savran, W. H., Werner, M. J., Marzocchi, W., Rhoades, D. A., Jackson, D. D.,
925 Milner, K., ... Michael, A. (2020). Pseudoprospective evaluation of UCERF3-
926 ETAS forecasts during the 2019 Ridgecrest sequence. *Bull. Seismol. Soc. Am.*,
927 110(4), 1799-1817. doi: 10.1785/0120200026
- 928 Schorlemmer, D., Gerstenberger, M. C., Wiemer, S., Jackson, D. D., & Rhoades,
929 D. A. (2007). Earthquake likelihood model testing. *Seismol. Res. Lett.*, 78(1),
930 17-29. doi: 10.1785/gssrl.78.1.17
- 931 Schorlemmer, D., Werner, M. J., Marzocchi, W., Jordan, T. H., Ogata, Y., Jackson,

- 932 D. D., ... Zhuang, J. C. (2018). The collaboratory for the study of earth-
 933 quake predictability: Achievements and priorities. *Seismol. Res. Lett.*, *89*(4),
 934 1305-1313. doi: 10.1785/0220180053
- 935 SCSN. (2020). *Southern California Seismic Network*. <https://service.scedc>
 936 [.caltech.edu/eq-catalogs/date_mag_loc.php](https://service.scedc.caltech.edu/eq-catalogs/date_mag_loc.php). (last accessed: 2020-12-01)
 937 doi: 10.7909/C3WD3xH1
- 938 Shcherbakov, R., Goda, K., Iwanian, A., & Atkinson, G. M. (2013). Aftershock
 939 statistics of major subduction earthquakes. *Bull. Seismol. Soc. Am.*, *103*(6),
 940 3222-3234. doi: 10.1785/0120120337
- 941 Shcherbakov, R., Nguyen, M., & Quigley, M. (2012). Statistical analysis of the 2010
 942 Mw 7.1 Darfield earthquake aftershock sequence. *New Zealand J. Geol. Geo-*
 943 *phys.*, *55*(3), 305-311. doi: 10.1080/00288306.2012.676556
- 944 Shcherbakov, R., & Turcotte, D. L. (2004). A modified form of Båth's law. *Bull.*
 945 *Seismol. Soc. Am.*, *94*(5), 1968-1975. doi: 10.1785/012003162
- 946 Shcherbakov, R., Turcotte, D. L., & Rundle, J. B. (2004). A generalized Omori's law
 947 for earthquake aftershock decay. *Geophys. Res. Lett.*, *31*(11), L11613. doi: 10
 948 .1029/2004GL019808
- 949 Shcherbakov, R., Turcotte, D. L., & Rundle, J. B. (2005). Aftershock statistics. *Pure*
 950 *Appl. Geophys.*, *162*(6-7), 1051-1076. doi: 10.1007/s00024-004-2661-8
- 951 Shcherbakov, R., Turcotte, D. L., & Rundle, J. B. (2006). Scaling properties of the
 952 Parkfield aftershock sequence. *Bull. Seismol. Soc. Am.*, *96*(4B), S376-384. doi:
 953 10.1785/0120050815
- 954 Shcherbakov, R., Turcotte, D. L., & Rundle, J. B. (2015). Complexity and earth-
 955 quakes. In H. Kanamori (Ed.), *Earthquake seismology* (2nd ed., Vol. 4, p. 627-
 956 653). Elsevier.
- 957 Shcherbakov, R., Yakovlev, G., Turcotte, D. L., & Rundle, J. B. (2005). Model
 958 for the distribution of aftershock interoccurrence times. *Phys. Rev. Lett.*, *95*,
 959 218501. doi: 10.1103/PhysRevLett.95.218501
- 960 Shcherbakov, R., Zhuang, J., & Ogata, Y. (2018). Constraining the magnitude of the
 961 largest event in a foreshock-mainshock-aftershock sequence. *Geophys. J. Int.*,
 962 *212*(1), 1-13. doi: 10.1093/gji/ggx407
- 963 Shcherbakov, R., Zhuang, J., Zöller, G., & Ogata, Y. (2019). Forecasting the mag-
 964 nitude of the largest expected earthquake. *Nat. Commun.*, *10*, Art. 4051. doi:

- 965 10.1038/s41467-019-11958-4
- 966 Shearer, P. M. (2012). Self-similar earthquake triggering, Båth's law, and fore-
 967 shock/aftershock magnitudes: Simulations, theory, and results for southern
 968 California. *J. Geophys. Res.*, *117*, B06310. doi: 10.1029/2011jb008957
- 969 Shebalin, P., Narteau, C., & Baranov, S. V. (2020). Earthquake productivity law.
 970 *Geophys. J. Int.*, *222*(2), 1264-1269. doi: 10.1093/gji/ggaa252
- 971 Shebalin, P., Narteau, C., Holschneider, M., & Schorlemmer, D. (2011). Short-term
 972 earthquake forecasting using early aftershock statistics. *Bull. Seismol. Soc.*
 973 *Am.*, *101*(1), 297-312. doi: 10.1785/0120100119
- 974 Tahir, M., Grasso, J. R., & Amorese, D. (2012). The largest aftershock: How strong,
 975 how far away, how delayed? *Geophys. Res. Lett.*, *39*, L04301. doi: 10.1029/
 976 2011gl050604
- 977 Taroni, M., Marzocchi, W., Schorlemmer, D., Werner, M. J., Wiemer, S., Zechar,
 978 J. D., ... Euchner, F. (2018). Prospective CSEP evaluation of 1-day, 3-month,
 979 and 5-yr earthquake forecasts for Italy. *Seismol. Res. Lett.*, *89*(4), 1251-1261.
 980 doi: 10.1785/0220180031
- 981 Tinti, S., & Mulargia, F. (1987). Confidence intervals of *b*-values for grouped magni-
 982 tudes. *Bull. Seismol. Soc. Am.*, *77*(6), 2125-2134.
- 983 Toda, S., & Stein, R. S. (2020). Long- and short-term stress interaction of the 2019
 984 Ridgecrest sequence and Coulomb-based earthquake forecasts. *Bull. Seismol.*
 985 *Soc. Am.*, *110*(4), 1765-1780. doi: 10.1785/0120200169
- 986 USGS. (2006). *U.S. Geological Survey and California Geological Survey quaternary*
 987 *fault and fold database*. <https://earthquake.usgs.gov/hazards/qfaults/>.
 988 (last accessed: 2020-07-01)
- 989 Utsu, T. (1961). A statistical study on the occurrence of aftershocks. *Geophys.*
 990 *Mag.*, *30*, 521-605.
- 991 Utsu, T., Ogata, Y., & Matsu'ura, R. S. (1995). The centenary of the Omori formula
 992 for a decay law of aftershock activity. *J. Phys. Earth*, *43*(1), 1-33.
- 993 Vere-Jones, D. (1969). A note on the statistical interpretation of Båth's law. *Bull.*
 994 *Seismol. Soc. Am.*, *59*, 1535-1541.
- 995 Vere-Jones, D. (1975). Stochastic models for earthquake sequences. *Geophys. J. Int.*,
 996 *42*(2), 811-826. doi: 10.1111/j.1365-246X.1975.tb05893.x
- 997 Vere-Jones, D. (2010). Foundations of statistical seismology. *Pure Appl. Geophys.*,

- 998 167(6-7), 645-653. doi: 10.1007/s00024-010-0079-z
- 999 Werner, M. J., Helmstetter, A., Jackson, D. D., & Kagan, Y. Y. (2011). High-
1000 resolution long-term and short-term earthquake forecasts for California. *Bull.*
1001 *Seismol. Soc. Am.*, 101(4), 1630-1648. doi: 10.1785/0120090340
- 1002 Zechar, J. D., Gerstenberger, M. C., & Rhoades, D. A. (2010). Likelihood-based
1003 tests for evaluating space-rate-magnitude earthquake forecasts. *Bull. Seismol.*
1004 *Soc. Am.*, 100(3), 1184-1195. doi: 10.1785/0120090192
- 1005 Zöller, G., Holschneider, M., & Hainzl, S. (2013). The maximum earthquake mag-
1006 nitude in a time horizon: Theory and case studies. *Bull. Seismol. Soc. Am.*,
1007 103(2A), 860-875. doi: 10.1785/0120120013